The Cofilin Activity Pathway in Metastasizing Mammary Tumour Cells

by

Erin Prosk

B.Sc., McGill University, 2007

A THESIS SUBMITTED IN PARTIAL FULFILLMENT OF
THE REQUIREMENTS FOR THE DEGREE OF

MASTER OF SCIENCE

in

The Faculty of Graduate Studies

(Mathematics)

THE UNIVERSITY OF BRITISH COLUMBIA

(Vancouver)

August 2009

Abstract

The activity of cofilin has been identified as a critical determinant of the metastatic potential of carcinoma cells *in vivo* [15, 23]. The burst cofilin-mediated barbed end production following stimulation of a cancer cell with EGF is not yet completely understood [7, 24]. This motivates the use of mathematical models to test experimental hypotheses and propose areas for future experimental consideration.

In this thesis, I outline the initial temporal models of the cofilin activity pathway in metastasizing mammary tumour cells developed by myself and my supervisor Leah Edelstein-Keshet. This work results from a collaboration with experimentalist Dr. John Condeelis (Albert Einstein College of Medicine of Yeshiva University). The project is hierarchical, building from a reduced model of cofilin-barbed end interaction (Chapter 2), to include distinct cofilin forms (Chapter 3) and compartmental considerations (Chapter 4). In each model, we investigate essential mechanisms of the cofilin pathway required to reproduce the barbed end peak observed in experiment. The models presented in Chapters 2-4 represent the initial step in the modeling analysis of the cofilin activity pathway. The work serves to validate current hypotheses about the cofilin activity pathway and identify important interactions and considerations for future experimental and theoretical development.

Table of Contents

List of Tables

List of Figures

Acknowledgements

This work is part of a very wonderful experience in graduate studies at UBC. I would like to thank the Department of Mathematics and the Institute of Applied Math for the incredible support, amazing learning opportunities, and stimulating working environment. I appreciate the many interesting and helpful discussions with members of the Math Biology group, visitors and other colleagues, including Sasha Jilkine, Stan Maree, and Jacco van Rheenen. Thank you to our collaborator John Condeelis for his invaluable contributions to the project. I would like to thank my research supervisor Leah Edelstein-Keshet for her unwavering support, enthusiasm and patience. Thank you to the IGTC Math Biology Program for the financial support to make my graduate experience possible.

Chapter 1

Introduction

1.1 Cell Motility

Directed cell motility is a fundamental process in many biological and pathological contexts. In human physiology, cell movement encompasses such critical processes as cellular differentiation during embryogenesis, chemotaxis of immune cells, fibroblast migration during wound healing, and invasion and metastatic behaviour of tumour cells. Each of these processes demands the ability of a cell to detect and respond to external signals quickly and with relative precision.

Playing such a critical role in the maintainence of biological and physiological well-being, cell motility has been stationed at the forefront of both experimental and theoretical study for many years. However, much of this work has been focused on the motility of biological systems, chemotaxis of amoeboid *Dictyostelium* cells and fish keratocytes. These cell types, and their mechanism of movement are inherently different than the human physiological counterparts of which a surprisingly small number of systems have been studied extensively.

Most surprisingly, theoretical modeling of the migration and invasion of cancer, our population's leading cause of death, has seen little attention until recently. Consequently, the cellular mechanisms causing and driving the progression of this dangerous disease are very poorly understood. Modern advancements in fluorescence microscopy imaging and parallel work in the analysis of genetic networks which determine metastatic potential of tumour cells have shone light onto the cellular pathways important for metastatic behaviour. These recent experimental discoveries demand theoretical analysis to expand on previous cell motility theories in light of the experimentally predicted similarities and distinct differences of cancer cell migration. Such understanding will be critical to determine the important cellular targets to prevent invasive

migration of cancerous cells.

General cell movement occurs by fine coordination of several distinct and important steps. Cells initiate protrusion at the front in response to an external stimulus. They attach to available substrate at the site of protrusion before contracting at the back and releasing their trailing edge. This process is repeated as the cell moves in the direction of protrusion toward an external stimulus. It is a fundamental sequence of events consistent across the wide range of motile cells. In each case, the initial step in the motility cycle requires the sensing of chemotactic signals by receptors on the surface of the cell. The activation is relayed to the interior of the cell, kicking off a complex signaling pathway. Activity culminates in polymerization of new actin at the front of the cell, generating a protrusive force to extend the membrane in the direction of motion. In this manner, the activity of the signaling pathway determines the directionality of cell movement by designating the location of the initial protrusion.

The goal of this thesis is to examine one such signaling pathway, the cofilin activity cycle, which has been recently identified as a key component of the metastatic phenotype of mammary tumour cells [15, 29, 32]. This work is the result of a collaboration with Dr. John Condeelis, an experimental cell biologist, professor and co-chair of the Department of Anatomy and Structural Biology at the Albert Einstein College of Medicine of Yeshiva University. His research lab has produced much of the recent experimental literature of breast cancer study *in vivo*, and supports the important role of the cofilin activity cycle.

The inherent complexity of cancer cell study *in vivo* limits the extent of experimental understanding. Discussions with John Condeelis identified the importance of deciphering an early peak of barbed end density produced by the stimulated activity cycle and critical to the directed migration of cancer cells. The current experimental shortcomings motivate our initial modeling efforts. We focus initially on reproducing the barbed end peak by examining the underlying cofilin interactions in a simplified, temporal framework. We hope to gain insight into the important interactions within the cofilin activity cycle, however, determining model parameters is a major challenge toward accurate representation of the system. This thesis outlines the important initial step in the analysis of the primary regulators of cancer cell metastasis. The work

described here helps to simplify the complex spatiotemporal system and provide a foundation for later models. In the next section, I will motivate our recent modeling efforts by describing some experimental work from the Condeelis Lab.

1.2 Review of Actin Dynamics

Actin exists in the cell in two very closely linked forms. As long, thin filaments, actin comprises the primary component of the cell's cytoskeleton. The filaments are crosslinked into a network of structural scaffolding determining cell shape and maintaining mechanical properties, internal force and resistance within the cell.

The cytoskeleton and each individual filament are dynamic structures constantly polymerizing and depolymerizing via addition or loss of the monomer form of the protein, G-actin. G-actin diffuses freely in the cell and associates to the nucleotide ATP in the cytosol which hydrolyzes over time to ADP. Actin filaments are polar structures with distinctly higher monomer addition rates and an affinity to ATP-bound G-actin at their barbed ends, and increased rate of monomer dissociation of ADP-bound G-actin at the pointed ends. In this manner, polymerizing actin filaments will exhibit a newly formed cap of ATP-actin at the free "barbed end" with a tail of older ADP-bound monomers trailing to the disassembling "pointed end". An extensive analysis of the dynamics of the actin forms and associated actin binding proteins has been studied in Mogilner and Edelstein-Keshet (2002) [21].

The dynamics of the actin cytoskeleton are controlled by a complex network of signalling pathways in the cell. The activity of these networks can be spatially separated, allowing a cell to polarize in response to an external signal. Signalling molecules such as phosphoinositides and Rho proteins can influence the activity of local actin binding proteins (ABPs) which up or downregulate actin polymerization in a local region of the cell. Some ABPs, which upregulation actin, do so by creating additional polymerizing barbed ends. The enhanced polymerization generates force against the membrane and causes the cell to protrude at the site of activity.

The cell has three general mechanisms to create new free barbed ends: (1) uncapping of inhibited barbed ends by release of capping protein or release of bound gelsolin [18, 30], (2) nu-

cleation of new filaments by the Arp2/3 complex [26], or (3) severing of existing older filaments by cofilin [7].

The activity of these proteins is tightly regulated in a cell to maintain dynamic stability of the actin cytoskeleton. The regulation of each protein can occur via pathways which are strongly interconnected, or by independent mechanisms, depending on the cell type studied and on the system of chemoattractant sensing within the cell. Here we study the regulation of just one such protein, the control of cofilin activity in the rat MTLn3 mammary adenocarcinoma cell line, an experimental model for the study of breast cancer cells.

1.2.1 Role of Cofilin

As cancer develops in the body, carcinoma cells undergo many stages of mutations. Early cell mutations increase proliferation at the cancer site, creating tumours. As the disease progresses, later mutations promote the abnormal migration of these normally non-motile cells, which can metastasize, or invade blood vessels causing the disease to spread to other tissues. The activity status of cofilin has been shown to be distinctly different between strictly proliferating non-motile tumour cells and those which exhibit metastatic potential [24, 32]. Furthermore, recent work *in vivo* has identified that local cofilin activity is necessary for directional sensing and determines direction of cell motility [15, 23].

Cofilin binding to actin filaments occurs via its Ser-3 binding site. Under certain cellular conditions, the filament-bound cofilin can instill sufficient force on the filament to create a break. Cofilin associates to older segments of actin filaments where monomers are ADP-associated. This means that unlike binding and nucleation activity of the Arp2/3 complex, filament severing by cofilin is not restricted to the newly assembled filament cap, and does not require filaments to be actively polymerizing at all. Cofilin can bind and sever a capped mother filament, creating a new barbed end site for polymerizing of the daughter filament. This introduces the possibility of synergistic interactions between cofilin and Arp2/3 activity whereby the recently severed and polymerizing filament tips produced by cofilin are available for Arp2/3 nucleation [13].

Cofilin has been shown *in vitro* to bind filaments cooperatively [1, 3, 11]. This behaviour

is yet to be proven in living cells. However, cooperative effects are expected to occur due to the increased torsional flexibility of actin filaments upon cofilin binding [27]. It is strongly hypothesized by experimentalists that between 5 and 7 bound cofilin molecules are required *in vivo* to generate sufficient force to create a break (informal discussions with J. Condeelis and J. van Rheenen). This is supported by studies that examine structural force dynamics of cofilin binding [1, 27].

Inactivation of cofilin occurs by inhibition of the Ser-3 site, preventing binding to actin filaments and any consequent severing activity [22]. Cellular cofilin binds both G-actin monomers, and phosphate molecules at the same Ser-3 site with high affinity [28, 31]. Furthermore, cofilin is known to bind PIP_2 at the membrane of a cell. Structural studies have shown the PIP_2-binding site to overlap with the filament binding Ser-3 site [16]. In this manner, cellular cofilin can be inactivated, that is, its filament-severing activity is inhibited, by monomer-binding, phosphorylation, and PIP_2-binding at the membrane. These inactive forms of cofilin are relatively stable in a resting cell. In general, reactivation of cofilin requires a recycling process involving cellular complexes to strip monomers (SSH or CIN), facilitate dephosphorylation (LIM kinase) or cleave PIP_2 (PLC-γ).

Gradient sensing and chemotaxis of tumour cells is hypothesized to occur via a local excitation, global inhibition (LEGI) model [23, 25, 34]. Local activation of cofilin activity has been shown to occur by a PLC-mediated release of PIP_2-bound cofilin at the membrane of the cell [33], and is not spatially or temporally correlated to dephosphorylation [31]. Upon stimulation with chemoattractant, epidermal growth factor, or EGF, LIM kinase activity increases globally in the cell, increasing the phosphorylation and deactivation of cofilin [31]. Such a LEGI model facilitates a tight control of protrusion sites and allows the cell to accomplish precise directional sensing.

The cofilin activity pathway of metastasizing tumour cells is well motivated and explained in the recent review by van Rheenen et. al (2009) [32]. We use the qualitative structure described in Figure 1.1 together with data from recent experimental work (outlined in the Section 1.3) to quantify cellular interactions and underlying mechanisms of the observed burst of barbed end

density. These initial simple models provide a framework on which to extend further work in the field.

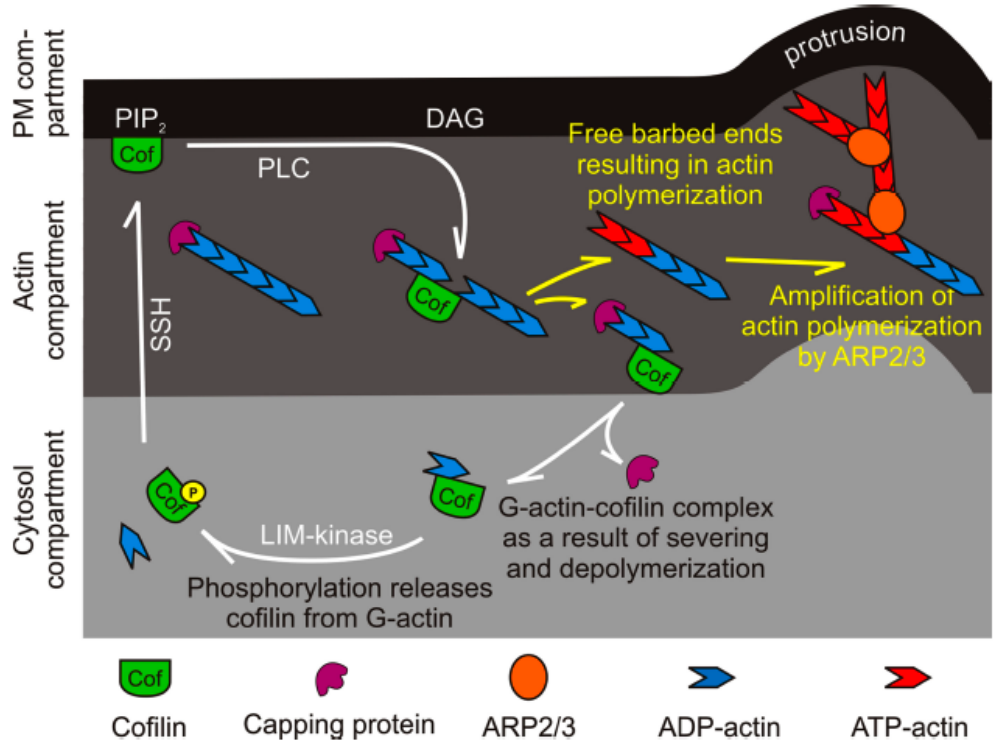

Figure 1.1: Cofilin molecules cycle through three compartments in the cell; the cytosol, the actin, and the PM compartments. Cofilin at the membrane (PM compartment) initially translocates to the F-actin compartment upon EGF mediated PIP_2 reduction. Cofilin binds and severs actin filaments resulting in filaments with free barbed ends, and cofilinG-actin complex. The cofilinG-actin complex cannot bind actin or PM, and therefore diffuses to the cytosol compartment. In the cytosol compartment, cofilin is phosphorylated by LIM-kinase (LIMK), resulting in the release of cofilin from the cofilinG-actin complex. Upon cofilin dephosphorylation by SSH, cofilin can reenter the membrane (PM) or F-actin compartment, starting a new cycle. The cycling of cofilin through the three compartments increases free barbed ends, resulting in newly polymerized actin filaments. The Arp2/3 complex prefers to bind to these newly formed actin filaments, which amplifies the cofilin-induced actin polymerization, resulting in protrusion formation [32, 33]. Reprinted with permission from J van Rheenen: EGF-induced PIP_2 hydrolysis releases and activates cofilin locally in carcinoma cells. *Journal of Cell Biology* 179(6):1247-59 (2007).

1.3 Review of Experimental Data

Recent work has identified and quantified the impact of cofilin activity in the rat MTLn3 carcinoma cell line. This cell type has been chosen for study due to the PLC-dependency of cofilin-induced barbed end formation, protrusion and chemotaxis [23], and the correlation of cofilin activity with the metastatic potential of the cell [34].

Experimental work utilizing recent developments in multiphoton fluorescence imaging and MTLn3 cell properties has demonstrated the critical role of the cofilin pathway in invasive tumour cells *in vivo*. The cycle initiates via an increase in activity of PLC-γ in the membrane of the cell upon EGF stimulation [24]. This induces a rapid and significant reduction of PIP_2 into diacylglycerol (DAG) and inositoltrisphosphate (IP_3) in the membrane.

Cofilin has been shown to be in rapid equilibrium with PIP_2 in a strong and stable configuration at the membrane of a cell. This relatively high fraction of cellular cofilin is reduced significantly upon EGF stimulation. The experimental time profiles of these phenomena are shown in Figure 1.2. We use these to fit PLC and PIP_2 dynamics of our models described in Chapters 3 and 4 of this thesis.

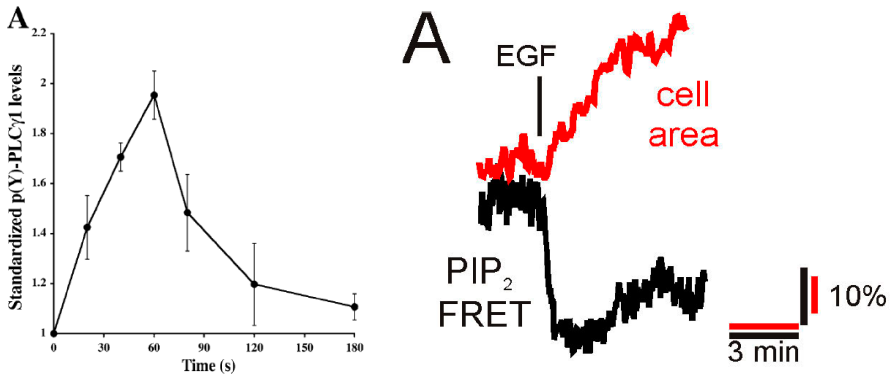

Figure 1.2: Left: Dynamics of PLC from Figure 2 A of Mouneimne (2004) [24]. Right: Dynamics of PIP_2 from Figure 1 A of van Rheennen (2007) [33]. Reprinted with permission from G Mouneimne: Phospholipase C and cofilin are required for carcinoma cell directionality in response to EGF stimulation. *Journal of Cell Biology* 166(5):697-708 (2004), and J van Rheenen: EGF-induced PIP_2 hydrolysis releases and activates cofilin locally in carcinoma cells. *Journal of Cell Biology* 179(6):1247-59 (2007).

Until recent developments in microscopy, cofilin dynamics were studied *in vitro* where cellular interactions and pathway dynamics may be significantly different. Consequently, though the dynamics we study here are strongly supported by experimental studies [32], the collection of quantified temporal data of cofilin in its various cellular forms is less complete. We are cautious of using the extensive *in vitro* library of work to validate our model. Much of the study of filament binding dynamics, especially the extensive analysis of cofilin binding and severing actin filaments has been under *in vitro* conditions [1, 4, 11, 17].

Instead, we focus on the filament binding data described in van Rheenen (2007) where cofilin is released from the membrane upon EGF stimulation, and binds rapidly to membrane-associated filaments ($< 200n$m from the membrane) [33]. We work under the assumption motivated by data in van Rheenen (2007), whereby filament-bound cofilin increases less than two-fold following stimulation with EGF. This is shown in Figure 1.3.

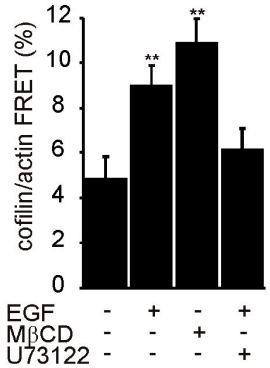

Figure 1.3: Relative increase in filament-bound cofilin at 0s and 60s following stimulation with EGF, from Figure 5 A of van Rheennen (2007) [33]. Reprinted with permission from J van Rheenen EGF-induced PIP_2 hydrolysis releases and activates cofilin locally in carcinoma cells. *Journal of Cell Biology* 179(6):1247-59 (2007).

As described in previous sections, this relatively small fold increase in cofilin activity (in the form of bound cofilin) induces an amplification of barbed end production in the cell. Within 60s following stimulation with EGF, the relative number of free polymerizing barbed ends in the cell increases to a magnitude up to a 12-fold greater than the barbed end density at rest [24]. This increase is highly dependent on experimental conditions such as temperature, and pH changes induced by the activity of other signaling networks in the cell, The increase in barbed

end density is stated as an average of 2.7 and 3.2 fold increases in other studies [15, 19]. Within a simple modeling framework, we attempt to reproduce these quantified barbed end amplifications. An example of maximal barbed end amplification, for optimal cellular conditions is shown in Figure 1.4, from Mouneimne (2004) [24].

The early peak of barbed end density at 60s following stimulation with EGF has been shown to be a product of PLC-mediated cofilin activity in the cell. The later peak, at 180s after stimulation, is dependent on the Arp2/3 pathway regulated by PI3 kinase (PI3K) in both amoeboid *D. discoideum* and carcinoma cells [8]. Figure 1.5 exhibits this phenomenon by quantifying barbed ends, under two conditions: control vs PLC-inhibited. The early peak of barbed ends is cofilin dependent and is sufficient to determine direction of cell motility in carcinoma cells. This motivates the focus our attention on the analysis of the cofilin pathway and resulting peak of barbed end density 60s following stimulation with EGF [15].

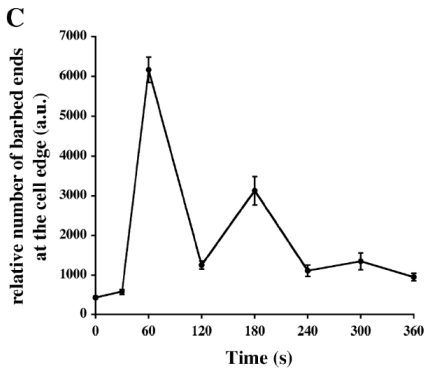

Figure 1.4: Relative increase in barbed end density by quantifying ATP-actin fluorescence increase at the leading edge of the cell, from Figure 1 C of Mouneimne (2004) [24]. Reprinted with permission from G Mouneimne: Phospholipase C and cofilin are required for carcinoma cell directionality in response to EGF stimulation. *Journal of Cell Biology* 166(5):697-708 (2004).

The experimental data outlined here, together with the hypothesized cofilin interactions in the pathway outlined in the recent review from van Rheenen et. al (2009) forms the foundation of our model development [32]. The following chapters describe the initial analysis of the pathway dynamics. In each case, we use the relevant data shown in the figures here to fit parameters, and both motivate and validate model assumptions.

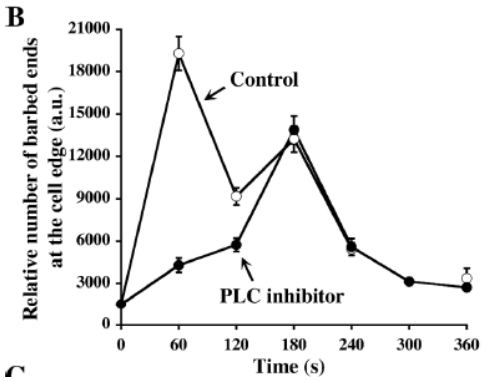

Figure 1.5: Relative increase in barbed ends at the cell edge under control and PLC-inhibited conditions from Figure 3 B of Mouneimne (2004) [24]. Reprinted with permission from G Mouneimne: Spatial and temporal control of cofilin activity is required for directional sensing during chemotaxis. *Current Biology* 16(22):2193-205 (2006).

In the following chapters, I will describe our efforts to quantify the effect of the cofilin activity cycle on the actin cytoskeleton at the leading edge. The models are hierarchical, expanding from a simple reduced cofilin-barbed end model, to a complex model framework describing interactions between distinct cofilin forms and transitions between cellular compartments. Chapter 2 first describes a reduced model which examines the interaction between the density of a single cofilin form, termed active cofilin for its filament severing ability, and production of barbed ends. Chapter 3 introduces a closed temporal model of cofilin transitioning between various forms in a well-mixed cell, and the consequent impact on cytoskeletal dynamics. Finally, Chapter 4 expands the cofilin cycle model to include some spatial considerations by dividing the cell into edge and interior compartments, while still maintaining temporal dynamics in the equations. I will also outline the different levels of complexity in the number of cofilin interactions we have examined in each model. Finally, in Chapter 5, I will discuss the conclusions made from this work, and the proposed areas for both experimental and theoretical future study.

Chapter 2

Reduced Cofilin Barbed End Model

2.1 Motivation

Cofilin is known to sever filaments under specific cell conditions. The severing events create an increase in free barbed ends which can polymerize and create protrusive forces. It has been shown that cofilin activity is directly linked to spatial localization of directed movement of the cell [15]. In this chapter, I outline our examination of the relationship between cofilin activity and free barbed ends with a simplified model. Using the information outlined in Section 1.3, we attempt to reproduce the signal amplification using a variety of modeling techniques to capture the biological properties of the cofilin activity cycle.

2.2 Barbed End Model

Under the most general and simplest considerations, free, polymerizing barbed ends are produced by a variety of actin-binding proteins, including cofilin, in the cell. The rate of barbed end production is tightly regulated in a resting cell, such that the base production rate $P_{B,rest}$ can be considered constant. Growing barbed ends are lost due to binding of capping proteins at a rate proportional to barbed end density. We consider a constant capping rate, k_{cap} based on a near constant lifetime of barbed ends in the cell, $k_{cap} \approx 1s^{-1}$ [26]. We define barbed end density in the cell as $B(t)$, expressed in units of number per μm^3. Barbed end dynamics in a resting cell are described by the proposed equation

$$\frac{dB}{dt} = P_{B,rest} - k_{cap}B. \tag{2.1}$$

This allows a simple identification of the resting steady state level of barbed ends, since if $\dot{B} = 0$, then

$$B_{rest} = \frac{P_{B,rest}}{k_{cap}}.$$

Without an applied stimulus, the system approaches this resting state asymptotically, from any initial level of barbed ends $B(0)$.

Suppose that upon stimulation, production of barbed ends increases from $P_{B,rest}$ to $P_{B,stim}$. Through the same analysis, the steady state barbed end level under stimulated conditions will be

$$B_{stim} = \frac{P_{B,stim}}{k_{cap}},$$

where $P_{B,stim} > P_{B,rest}$. Here we ignore any transition period between the two states of production, considering a stepwise increase in production rate from rest to stimulated conditions. This models an instantaneous increase in activity of actin-binding proteins in the cell. The stimulated steady state is also asymptotically stable, and barbed end levels will approach B_{stim} as long as the production rate remains at $P_{B,stim}$. If the stimulus is removed and barbed end production returns to the level $P_{B,rest}$, the barbed end density decreases back to B_{rest}.

The magnitude of increase in barbed end production and barbed end level is dependent on the ratio between resting and stimulated states since the condition

$$\frac{B_{stim}}{B_{rest}} \leq \frac{P_{B,stim}}{P_{B,rest}} \tag{2.2}$$

must be satisfied for all time. Thus, the ratio of production rates, $P_{B,stim}/P_{B,rest}$, determines the maximum amplification of barbed ends. Barbed end density will reach maximum amplification only if the stimulus is applied for sufficient time.

2.3 Cofilin Barbed End Model Details

Shown in Figure 1.2 in Section 1.3, EGF stimulation of MTLn3 cells can induce up to a 10-15 fold increase in barbed end density within $60s$ following stimulation. This has been shown to be dependent on the cofilin pathway and independent of the activity status of other ABPs in the

cell [13]. We define the cofilin concentration that is active in severing filaments as $C(t)$ usually expressed in units of μM. We propose the following general formulation for a mini model of cofilin and barbed ends

$$\begin{aligned} \frac{dC}{dt} &= f(C,B), \\ \frac{dB}{dt} &= g(C,B), \end{aligned}$$

where $B(t)$ is the density of barbed ends (usually in number per μm^2).

2.3.1 Cofilin Model Assumptions

- The early and late peaks of barbed end levels, at 60s and 180s following stimulus with EGF are dependent on cofilin and Arp2/3 respectively [13, 24]. The respective pathways are independent of one another, as shown in the data reprinted here in Figure 1.5 [13].
- Barbed ends are produced by the activity of actin-binding proteins in the cell at rest. There is no apparent feedback between barbed ends and their own rate of production (as discussed previously). The increase in barbed end production under stimulated conditions is assumed to be strictly due to increased activity of cofilin. Our simple barbed end equation (Equation 2.1) applies here with a cofilin-dependent barbed end production rate, $P_{B,stim} = P_{B,stim}(C)$.
- The observed 10-15 fold increase at $60s$ demands amplification upstream of the barbed end dynamics. We assume here that this stems from the activity of cofilin.
- Severing events occur at low frequency in resting cells as several (between 5-7) bound cofilin molecules are required to sever an actin filament. Cofilin has been shown *in vitro* to exhibit cooperative binding and severing properties [1, 11]. Following a severing event, cofilin molecules are left in an inactive, monomer-bound form which must be recycled on a longer time scale before being reactivated [31, 33].

In this simplified model, the cofilin concentration $C(t)$ (in μM) is in a form bound to the actin filaments, available to cut provided required conditions are met. We address distinct cofilin forms, active and inactive, in Chapters 3 and 4.

We identify that cofilin can be activated at some time dependent rate in the cell, $A_C(t)$, which we assume to be dependent on some external factor. Cofilin is deactivated at a rate $k_{off}C$ proportional to its concentration. We assume that cofilin also loses its activated status after a severing event at a rate dependent on its concentration $F_{sev}(C)$, as in Figure 1.1 from van Rheenen (2009), cofilin is released from the daughter filament in an inactive, monomer-bound form. We use a barbed end equation of a form similar to Equation 2.1. We introduce the production of barbed ends by cofilin severing at a rate proportional to the rate of cofilin loss $\alpha F_{sev}(C)$.

We propose the following system to represent interactions between cofilin activity and barbed ends in the cell

$$\begin{aligned} \frac{dC}{dt} &= A_C - k_{off}C - F_{sev}(C), \\ \frac{dB}{dt} &= P_B + \alpha F_{sev}(C) - k_{cap}B. \end{aligned} \tag{2.3}$$

Here $A_C = A_C(t)$ is the stimulus dependent activation rate of severing cofilin, k_{off} is a deactivation rate constant, $F_{sev}(C)$ is the cofilin-dependent severing rate which removes active cofilin from the system and increases barbed end density, α is a conversion factor between units of cofilin and barbed end density, and converts loss of cofilin activity into barbed end density produced (calculations shown in the Appendix).

We recognize that cofilin can be reactivated via a recycling process of inactivated cofilin, but we neglect this effect in this model as we consider this contribution to cofilin activity to be low within the relatively short time frame of the early barbed end peak [31, 33].

2.4 Linear Filament Severing

We propose a constant, basal level of cofilin activity in a resting cell, $A_{C,rest}$. We first examine a simple linear severing rate such that new barbed ends are produced at a rate proportional to the concentration of active cofilin

$$\begin{aligned} \frac{dC}{dt} &= A_C - k_{off}C - k_{sev}C, \\ \frac{dB}{dt} &= P_B + \alpha k_{sev}C - k_{cap}B. \end{aligned} \tag{2.4}$$

where k_{sev} is the severing constant. Based on this severing rate and Equations 2.4, the basal level of cofilin activity in a resting cell is

$$C_{rest} = \frac{A_{C,rest}}{k_{off} + k_{sev}}. \tag{2.5}$$

Cofilin activity increases upon stimulation with EGF [33]. We model this phenomenon by introducing temporal EGF dependence to the activation rate

$$A_C(t) = \begin{cases} A_{C,stim} \cdot EGF & \text{when stimulated by EGF,} \\ A_{C,rest} & \text{otherwise,} \end{cases} \tag{2.6}$$

where $A_{C,stim} \cdot EGF > A_{C,rest}$. While the EGF stimulus is switched on, the concentration of active cofilin approaches the stimulated steady state value

$$C_{stim} = \frac{A_{C,stim}}{k_{off} + k_{sev}}.$$

2.4.1 Analysis of Reduced Linear Model

Similar to the barbed end relationship described previously, under these assumptions the maximum increase in cofilin activity is dependent on the relative increase in activation rates

$$\frac{C(t)}{C_{rest}} \leq \frac{C_{stim}}{C_{rest}} = \frac{A_{C,stim}}{A_{C,rest}}.$$

Equations 2.4 imply a resting barbed end production rate

$$P_{B,rest} = P_B + \alpha \cdot k_{sev} C_{rest},$$

where $P_B > 0$ is the production of barbed ends by actin-binding proteins in the cell. The overall barbed end production increases upon stimulation to

$$P_{B,stim} = P_B + \alpha \cdot k_{sev} C_{stim}.$$

From Equations 2.4, the resting barbed end density is defined as

$$B_{rest} = \frac{P_B + \alpha k_{sev} C_{rest}}{k_{cap}}, \tag{2.7}$$

and stimulated steady state

$$B_{stim} = \frac{P_B + \alpha \cdot k_{sev} C_{stim}}{k_{cap}}.$$

Thus, the relative increase in barbed ends is bounded by the relationship

$$\frac{B(t)}{B_{rest}} \leq \frac{B_{stim}}{B_{rest}} = \frac{P_B + \alpha \cdot k_{sev} C_{stim}}{P_B + \alpha \cdot k_{sev} C_{rest}}.$$

In order to capture the 10-15 fold increase in barbed ends shown in Figure 1.4,

$$\frac{B(t)}{B_{rest}} \approx \text{10-15}.$$

However, from Figure 2 of van Rheenen (2007), shown in Figure 1.3 in Chapter 1, the cofilin activity, recognized as the concentration of cofilin that is filament-bound and ready to sever, increases only by 2-fold during the first $60s$ after EGF stimulation [33]. This restricts the magnification of barbed ends to be less than a 2-fold increase, since

$$\frac{B(t)}{B_{rest}} \leq \frac{P_B + 2 \cdot \alpha \cdot k_{sev} C_{rest}}{P_B + \alpha \cdot k_{sev} C_{rest}} \leq 2.$$

This analytic analysis suggests a limitation of the linear model. We predict that the model will fail to generate barbed end increases of of greater than two-fold for the applied two-fold increase in cofilin concentration. These predictions can be tested by model simulations.

2.4.2 Model Scaling and Parameter Analysis

We scale the reduced linear model, Equations 2.4, by their rest steady states, shown in Equations 2.5 and 2.7. After some algebra and simplifications, we obtain simplified equations in nondimensional variables, $C(t) = C_{rest} \cdot c(t)$ and $B(t) = B_{rest} \cdot b(t)$, to obtain simplified equations in nondimensional variables

$$\begin{aligned} \frac{dc}{dt} &= (k_{off} + k_{sev})[\tilde{A}_C - c] \\ \frac{db}{dt} &= Ak_{sev}[c-1] - k_{cap}[b-1] \end{aligned} \tag{2.8}$$

where k_{off}, k_{sev} are as described previously (in s^{-1}), $\tilde{A}_C = A_{C,stim}/A_{C,rest}$ is the scaled cofilin stimulation rate, and the scaling parameter A is

$$A = \frac{\alpha C_{rest}}{B_{rest}}.$$

These simplifications reduce the number of parameters required for simulations. We test a range of scaled stimulation rates to obtain cofilin fold increase of 1.2-2.0 upon stimulation, as suggested in van Rheenen (2007) (shown in Figure 1.3 of this thesis). We approximate the cofilin off-rate, k_{off}, to generate these cofilin profiles. We use a low severing rate parameter (k_{sev}) as motivated by discussions with J. Condeelis and similar to the predicted value *in vitro* [1, 11]. The parameter A is calculated from work shown in the Appendix and approximations from the literature [19, 26]. These values are summarized in Table 2.1

2.4.3 Simulation of Reduced Linear Model

Using the parameters outlined in Table 2.1, results of linear model simulations are shown in Figures 2.1 and 2.2. The barbed end dynamics follow the cofilin concentrations, but exhibit an increase of less than two-fold. This is governed by the low increase in the linear severing rate.

2.4.4 Time-Dependent Stimulation

A more accurate representation of the EGF-induced increase in cofilin activity can be obtained by applying a stimulation rate which is linearly time dependent. This introduces a more gradual

Parameter	Description	Value	Source
k_{off}	cofilin-filament unbinding	$1.5s^{-1}$	estimated in model
k_{sev}	cofilin severing rate	$0.011s^{-1}$	Andrianantoandro 2006 [1]
$\tilde{A}_{stim}$	scaled cofilin stimulation	0.1-5.0	van Rheenen 2007 [33]
k_{cap}	barbed end capping rate	$1s^{-1}$	Pollard 2000 [26]
A	scaling parameter	1000	Pollard 2000, Lorenz 2004 [19, 26]

Table 2.1: Parameter estimates for reduced Cofilin compartmental model with a linear severing rate function.

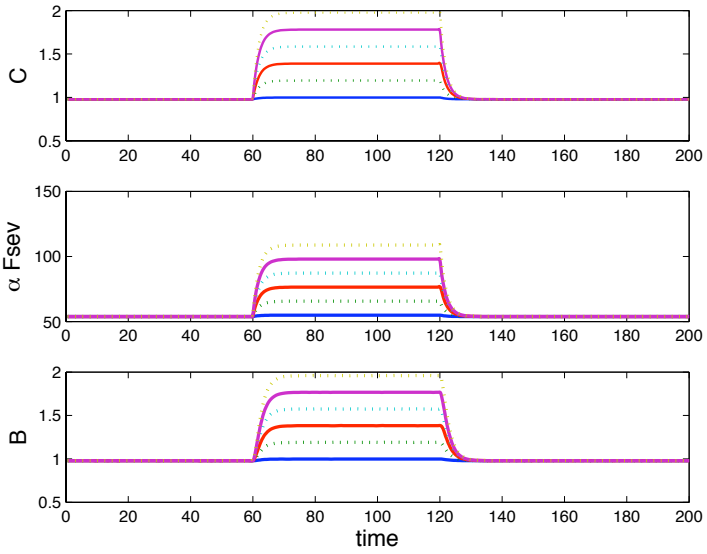

Figure 2.1: Results of simulations of Equations 2.8 with parameters as outlined in Table 2.1: time profiles of cofilin concentration relative to rest concentration (top curve), rate of actin filament severing (middle curve), and barbed end dynamics normalised by resting levels (bottom curve), with linear severing rate function. The stimulus is a step function $A_C(t)$ given by Equation 2.6, shown for increasing levels of stimulation $A_{stim} = 0.1, 1.0, 2.0, 3.0, 4.0, 5.0s^{-1}$.

increase in cofilin activity as observed in *in vitro* studies of cofilin binding to actin [1, 11]. The activation rate A_C (in s^{-1}) has the form

$$A_C(t) = \begin{cases} A_{C,stim}(t - t_{EGF}) \cdot EGF & \text{while EGF is on} \\ A_{C,rest} & \text{otherwise} \end{cases} \tag{2.9}$$

where $A_{C,stim} > A_{C,rest}$ and t_{EGF} represents the time of EGF stimulation.

The results of simulations, shown in Figures 2.3 and 2.4 are similar to previous step-function

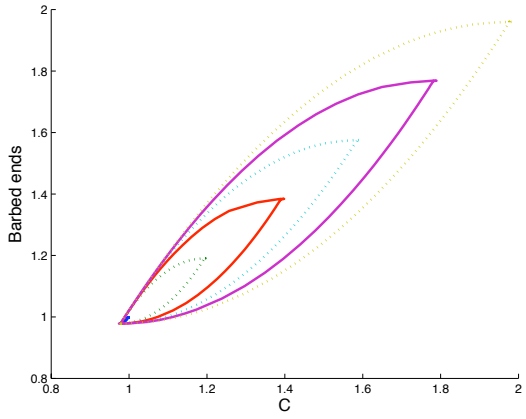

Figure 2.2: Phase space dynamics of cofilin activity and barbed end peak density (Equations 2.8 with parameters from Table 2.1), and linear severing rate function. Increases to the magnitude of stimulation, $A_{stim} = 0.1, 1.0, 2.0, 3.0, 4.0, 5.0 s^{-1}$, induce increases in magnitudes of cofilin concentration and barbed ends (loops in phase space).

stimulus, exhibiting very little amplification of barbed end density. The reduced model with linear severing rate is unable to generate the 10-12 fold barbed end amplification observed in experiment.

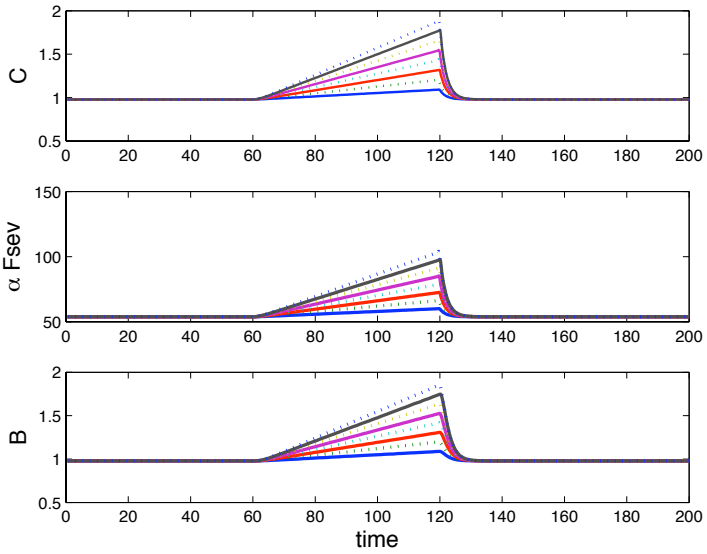

Figure 2.3: Results of simulations of Equations 2.8 with parameters as outlined in Table 2.1: Time profiles of cofilin (top curve), filament severing rate (middle curve) and barbed end dynamics (bottom curve), with linear severing rate function. The stimulus is applied as a linear function of time, see Equation 2.9, and scaled stimulation rate $\tilde{A}_{stim} = 0.001$-0.008.

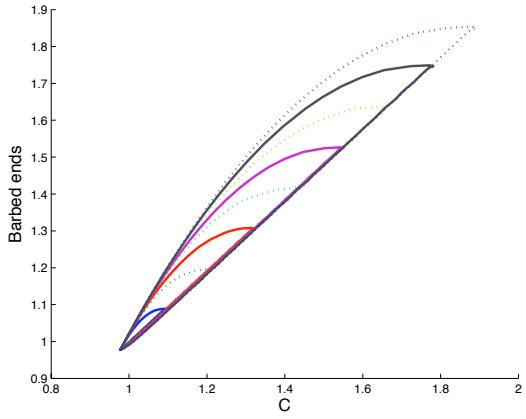

Figure 2.4: Phase space dynamics of cofilin activity and barbed end peak density (from Equations 2.8), with linear severing rate function and linear stimulus function with scaled stimulation $\tilde{A}_{stim} = 0.001\text{-}0.008 s^{-1}$.

2.5 Nonlinear Filament Severing

Based on the limitations of the cofilin model with linear severing rate, we propose a nonlinear severing rate as predicted by experimental work [1]. It has been identified that more than one bound cofilin molecule may be required to apply the torsional force necessary to create a break in an actin filament [27]. The kinetics of a such a severing event can be described by the simple schematic

$$nC + F \rightarrow B + nC_i,$$

where n is the number of molecules required to create a break, usually 5-7. The notation C_i represents an inactive form of cofilin, a product of a severing event, the dynamics of which will not be considered here.

These kinetics suggest the existence of a cooperative effect within the severing function, and motivate a nonlinear severing function. For example, consider a resting cofilin activity concentration where the equilibrium ready to sever state is 4 molecules per filament. Severing events would occur rarely at rest. An increase in the density of bound molecules upon stimulation to a state of 6 molecules per filament causes a substantial increase in severing frequency.

Typical biochemical assumptions motivate saturable kinetics in the form of a Hill function. We believe cofilin dynamics to be far from the region of saturation *in vivo*, and here use a severing rate proportional to C^n. Our examination of saturable kinetics is described briefly in Section 2.5.2, and provides supporting evidence for our assumptions.

We propose a nonlinear severing rate function where severing is low at rest conditions and increases when cofilin is elevated above rest concentrations. These conditions suggest an appropriate severing function for the cofilin-barbed end model in Equation 2.3 of the form

$$F_{sev}(C) = k_{sev} C_{rest} \left(\frac{C}{C_{rest}} \right)^n, \tag{2.10}$$

where $n \approx$5-7 and k_{sev} is a small constant. We assume the severing rate at rest, $F_{sev}(C_{rest}) = k_{sev} C_{rest}$ to be low.

Under these considerations, the cofilin-barbed end model takes the form

$$\begin{aligned} \frac{dC}{dt} &= A_C - k_{off}C - k_{sev}C_{rest}\left(\frac{C}{C_{rest}}\right)^n, \\ \frac{dB}{dt} &= P_B + \alpha k_{sev}C_{rest}\left(\frac{C}{C_{rest}}\right)^n - k_{cap}B.. \end{aligned} \tag{2.11}$$

At rest, barbed end production rate proposed earlier is of similar form

$$P_{B,rest} = P_B + \alpha \cdot k_{sev}C_{rest},$$

where if $k_{sev} << 1s^{-1}$, cofilin severing events are insignificant compared to the barbed end production by other actin binding proteins.

Notice that under such a model, even slight increases in cofilin activity above resting levels will be amplified so that here the stimulated severing rate is higher than the linear rate function for given resting severing rate k_{sev}. Solving for the resting steady state of active cofilin, we find the same relationship for rest state cofilin activity

$$C_{rest} = \frac{A_{C,rest}}{k_{off} + k_{sev}},$$

and at rest the barbed end density is

$$B_{rest} = \frac{P_B + \alpha \cdot k_{sev}C_{rest}}{k_{cap}}.$$

Similar to the procedure in the previous section, scaling Equations 2.11 by the resting concentrations of cofilin and barbed ends, so that $C = C_{rest} \cdot c$ and $B = B_{rest} \cdot b$, simplifying and rearranging terms, obtains the system

$$\begin{aligned} \frac{dc}{dt} &= k_{off}[\tilde{A}_C - c] + k_{sev}[\tilde{A}_C - c^n], \\ \frac{db}{dt} &= Ak_{sev}[c^n - 1] - k_{cap}[b - 1]. \end{aligned} \tag{2.12}$$

where $\tilde{A}_C = A_C/A_{C,rest}$ and steady states of these equations are now $c = 1$ and $b = 1$.

Expressed in this form, we notice the impact of the nonlinear severing rate. If the severing rate constant k_{sev} is low, as expected from experimental work [33], cofilin severing activity is low at rest conditions in the cell. Upon stimulation, $\tilde{A}_C > 1$, and cofilin activity increases above rest levels. This increases severing of filaments significantly and barbed end density is amplified. While the cofilin stimulus is turned on, the system is unstable and activity will increase exponentially, thereby causing exponential increase in barbed end density. This continues until the stimulus is removed and severing activity reduces back to basal resting level.

2.5.1 Simulation of Reduced Nonlinear Model

Simulations of Equations 2.4 are shown in Figures 2.5 and 2.6, with an applied nonlinear severing rate, linear stimulus as in Section 2.4.4, and with parameter values described in Table 2.2, can capture the 10-15 fold barbed end amplification. The amplification can be achieved with biologically reasonable parameter values and for increases in cofilin activity in the range of 1.5-2.0 fold increase. The results are robust to model parameters k_{off} and k_{sev}. The impact of the nonlinear assumption is exemplified in the profile of the function $\alpha F_{sev}(C)$. The magnitude of the severing rate, approximately one at rest conditions, increases several orders of magnitude with elevated cofilin activity. This generates the observed amplification of barbed end density.

This model represents a system far from saturation where filament-binding of cofilin is unlimited. The results can be viewed in the cofilin-barbed end phase plane Figure 2.6, where barbed end amplification is demonstrated with respect to cofilin activity. Notice increases in barbed end production are slight for cofilin activity just above resting levels. However, nonlinear effects take over as cofilin activity is increased up to the two-fold amplification .

Parameter	Description	Value	Source
k_{off}	cofilin unbinding	$1.5s^{-1}$	Pollard 2000 [26]
k_{sev}	cofilin severing parameter	$0.011s^{-1}$	Andrianantoandro 2006 [1]
$\tilde{A}_{stim}$	scaled cofilin stimulation	1-8·10^{-6}	van Rheenen 2007 [33]
n	cooperativity parameter	7	assumed in model
k_{cap}	barbed end capping rate	$1s^{-1}$	Pollard 2000 [26]
α	unit conversion factor	$600\mu M^{-1}\mu m^{-3}$	Mogilner, LEK 2002 [21]
A	scaling factor	1000	Pollard 2000, Lorenz 2004 [19, 26]

Table 2.2: Parameter estimates for reduced cofilin model with nonlinear, unsaturated severing rate function

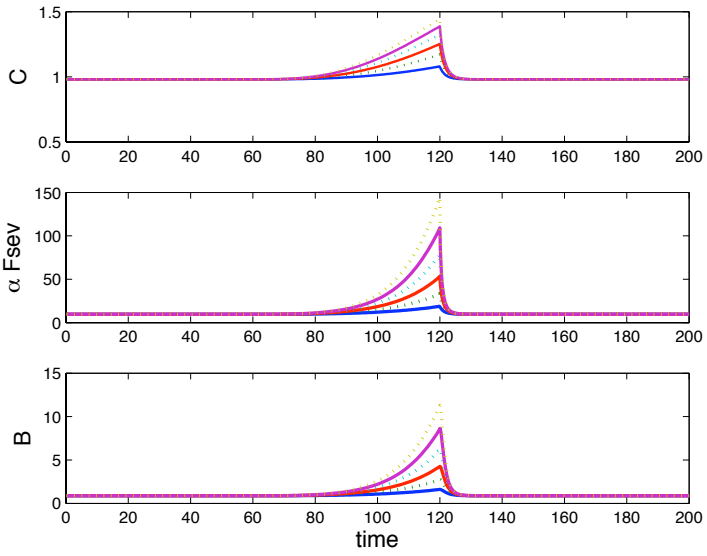

Figure 2.5: Results of simulations of Equations 2.12: Time profiles of cofilin concentration (top), scaled severing rate (middle), and barbed end density relative to basal levels(bottom) for nonlinear, unsaturated severing rate described in Section 2.5 with $k_{sev} = 0.011s^{-1}$, $\tilde{A}_C$ = 1-$8 \cdot 10^{-6}$ and other parameter values as outlined in Table 2.2

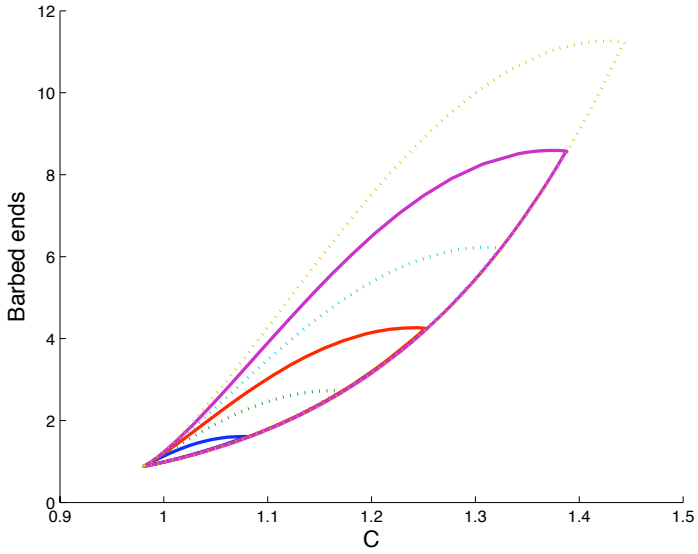

Figure 2.6: Phase plane dynamics of cofilin activity and barbed end density (from Equations 2.12) normalized by resting concentrations in the cell, with nonlinear, unsaturated severing rate with $k_{sev} = 0.011 s^{-1}$, $\tilde{A}_C = 1\text{-}8 \cdot 10^{-6}$ and other parameter values as outlined in Table 2.2

2.5.2 Nonlinear Filament Severing with Saturation

We considered the possibility of saturation in the dependence of actin filament severing on cofilin concentration. Saturable kinetics can be incorporated into the filament severing rate by introducing a Hill function of the form

$$F_{sev}(C) = \gamma_{max} k_{sev} C_{rest} \frac{C^n}{C^n + K}, \tag{2.13}$$

where $n = 7$ is the nonlinear factor or Hill coefficient, K is a saturation coefficient in units μM, and γ_{max} is a nondimensional parameter to scale the resting severing rate $k_{sev} C_{rest}$ of Section 2.5 to the saturated or maximum severing rate $\gamma_{max} k_{sev} C_{rest}$.

The reduced model can be scaled and simplified in terms of the saturable severing rate, following a similar procedure to that described in the previous section. Forgoing the algebraic details, we emphasize that under this severing rate assumption, barbed end amplification loses its robustness to parameters. Barbed end amplification in the 10-15 fold range is obtained strictly within a small window of the $\gamma_{max} k_{sev}$ parameter space. This range is shown in the left panel of Figure 2.7 where relatively high parameter settings are required (compared to experimental predictions [1, 11]).

The source of this model limitation is due to an increase in the severing rate at rest, and reduction of stimulated severing in certain parameter regions. This prevents increases of several orders of magnitude required to generate substantial amplification of barbed end density. The filament severing rate for rest concentration of cofilin is shown in the right panel of Figure 2.7 for the same range of parameter space.

The results of this applied severing rate, together with the experimental studies of filament binding concentrations and severing rates *in vitro* suggest that the increases in cofilin activity observed in living cells may be far from the potential regions of saturation. These conclusions suggest that the nonlinear severing rate described in Section 2.5 is a plausible severing function for future model expansions.

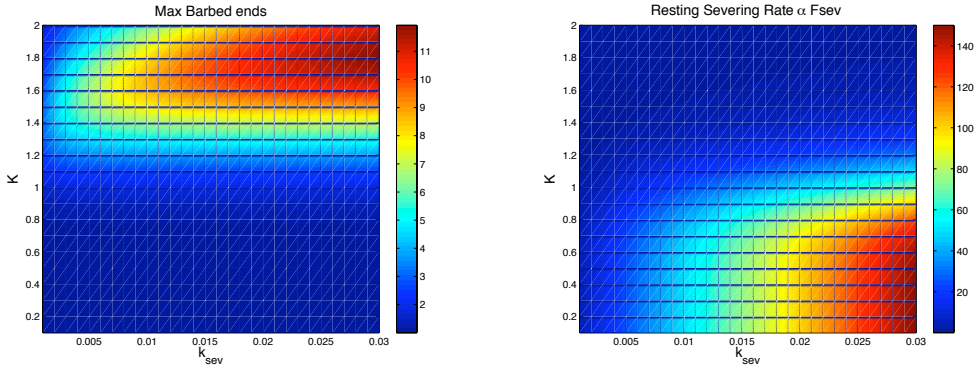

Figure 2.7: Results of simulation of barbed end model using saturated filament severing rate described in Section 2.5.2. Left: Maximum barbed end peak in parameter space of saturation coefficients K and combined severing rate constant $\gamma_{max}k_{sev}$. NOTE: x-axis labeled k_{sev} should be labeled $\gamma_{max}k_{sev}$ Right: Magnitude of scaled severing rate at rest conditions in the cell.

Chapter 3

Well-mixed Temporal Cofilin Model

3.1 Introduction

It has been shown that stimulation of an MTLn3 cell with EGF produces two large transient peaks of actin filament barbed end density. According to John Condeelis, and as outlined in several publications from his group [13, 24, 31, 32], the early transient peak at $60s$ after EGF stimulation is due to an increase in cofilin activity caused by a PLC-mediated release of PIP_2-bound inactive cofilin at the membrane of the cell (shown in Figure 1.5 in Section 1.3). The cofilin released upon stimulation is in an active form, ready to sever actin. It immediately translocates to bind to uninhibited membrane-associated actin filaments [33].

In this chapter, we expand the reduced cofilin activity model of Chapter 2 to analyse the dynamics of cofilin in its various cellular forms. We introduce cellular interactions and transitions between cofilin forms, some active in filament severing, others inactive, to quantify the mechanisms responsible for the observed cofilin-dependent protrusion. We follow the conclusions of the work in van Rheenen et. al (2007), and use recent supporting data to reproduce the observed peak of barbed ends. We apply the results of the reduced model of Chapter 2 to identify the filament-severing rate necessary to generate sufficient signal amplification.

We work with a closed model of the cofilin cycle, whereby cofilin exists in one of several proposed forms. We include slow recycling steps of the inactive cofilin forms via actin monomer-stripping and phosphorylation-dephosphorylation processes. These processes are facilitated by complexes including phosphatases such as SSH or CIN, and on LIM kinase (LIMK), but we will

consider constant complex activity here. We use temporal data of cofilin interactions to validate model assumptions where available. Following Figure 1.1 from van Rheenen (2007), we propose a temporal model of the cofilin cycle as outlined in Figure 3.1.

Cofilin Pool	Description	Resting Level	Source
C_2	PIP_2-bound cofilin	$0.10 \cdot C_{tot}$	van Rheenen 2007 [33]
C_A	active cofilin	$0.01 \cdot C_{tot}$	approximated in model
C_F	F-actin-bound cofilin	$0.02 \cdot C_{tot}$	van Rheenen 2007 [33]
C_M	G-actin-monomer-bound	$0.67 \cdot C_{tot}$	conservation assumption
C_P	phosphorylated cofilin	$0.20 \cdot C_{tot}$	Song 2006 [31]
C_{tot}	total cellular cofilin	$10\mu M$	Pollard 2000 [26]

Table 3.1: Definitions of the forms of cofilin modeled in this chapter with rest steady state concentrations

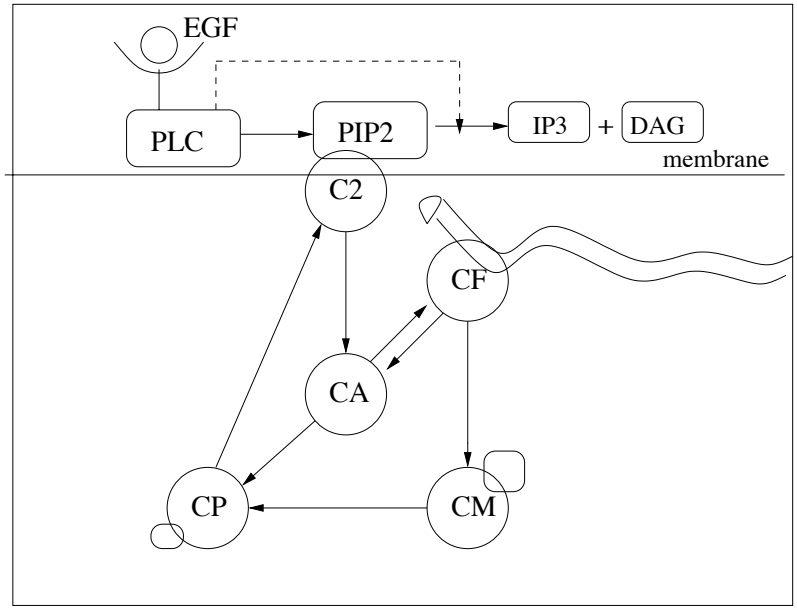

Figure 3.1: Schematic of proposed well-mixed temporal model of cofilin pathway: EGF stimulation activates PLC, causing the membrane lipid PIP_2 to be hydrolyzed. This releases the cofilin from the membranous PIP_2-bound pool (C_2) to an active form (pool C_A), from which it can attach to actin filaments (pool C_F). Once the filament is severed, cofilin comes off, carrying an actin monomer (pool C_M) with it. It is phosphorylated by LIM kinase into the form C_P, and then stripped of its monomer, so that it could reattach to PIP_2. Here we have also assumed that the active cofilin can exchange with the filament bound form or be phosphorylated.

3.1.1 Assumptions

Expanding on the assumptions of the reduced cofilin barbed end model of Chapter 2, we work with the following conditions.

- We consider here only temporal dynamics, and are thereby approximating the cell as a well-mixed system where cofilin concentrations are averaged across the cell, and molecules move freely between the cytosolic and peripheral compartments of the cell. In this model, we neglect spatial considerations.

- Cofilin is conserved in the system, so that cellular cofilin exists in one of the forms proposed here and their sum is constant, equal to the total concentration of cofilin in the cell. That is, for all time t, our system satisfies the equation

$$C_2(t) + C_A(t) + C_F(t) + C_M(t) + C_P(t) = C_{tot}. \tag{3.1}$$

  It is convenient to relate all cofilin pools to the fraction of total cofilin in the cell. Experimental data is expressed relative to average cofilin concentration C_{tot}, rather than in absolute concentrations. Scaling respective cofilin forms with respect to C_{tot}, such that $c_i(t) = C_{tot} \cdot C_i(t)$ obtains the dimensionless conservation equation

$$c_2(t) + c_a(t) + c_f(t) + c_m(t) + c_p(t) = 1, \tag{3.2}$$

  for all time t.

  At this point we neglect compartmental volume considerations, all cofilin forms are assumed to be well-mixed within the domain. This conservation equation will be examined and modified in further models. However, here we use this simple equation to gain rough insight into model behaviour.

- We assume that actin filaments are abundant and at constant density within the domain. We consider an actin binding rate dependent only on available cofilin, and combine the rate constant as $(k_{on}F)$. We assume filament severing to be independent of filament density.

- Stimulated production of barbed ends is assumed to be cofilin dependent. We assume, as

before, that barbed ends do not feed back on their own production. We use the equations proposed in Section 2.5 to govern barbed end dynamics.

3.2 Model Development

The model considered here is closely based on Figure 3.1. We identify the cofilin concentration active in filament-severing, C, of the reduced model, as the concentration of filament bound cofilin C_F, in this model framework. In this section, I motivate and describe the equations of component of the system. Readers can skip to Section 3.3 for a summary of model equations.

Under the simplest assumptions, for a resting cell, we consider basal rates of activation, I_G, and basal deactivation rates proportional to concentrations, $-d_G G$. A typical substance with concentration $G(t)$ would satisfy the equation

$$\frac{dG}{dt} = I_G - d_G G.$$

To such equations, we add various linear and nonlinear terms to account for interconversion and stimulation effects. Unless otherwise stated, component concentrations are measured in micro-molar values, (μM), where $1\mu M \approx 6 \cdot 10^{17} \text{molec} L^{-1}$. We also consider a closed system of cofilin, so that the sum of cofilin in all forms is a constant, as in Equation 3.1.

1. **Dynamics of PLC Activity:** We start analysis by quantifying phospholipase-C (PLC) activity and PtdIns(4,5)P2 (PIP_2) dynamics, as the experimental time profiles of these regulators are well-documented, shown in Figure 1.2. Furthermore, PLC activity represents the kicking-off point for our simulations, initiating the cascade of downstream transient states. We assume a basal level of production and decay of PLC activity in a resting cell. We introduce an enhanced production rate of active PLC, which is dependent on presence of an EGF stimulus. Once the EGF signal is turned off, the active PLC concentration settles down to its resting state, and consequently each cofilin pool returns to resting state on their respective time scales.

The proposed equation for PLC dynamics is

$$\frac{dPLC}{dt} = \underbrace{I_{stimPLC}(t)}_{stimulated\ activation} + \underbrace{I_{PLC} - d_{PLC}PLC}_{basal\ rates}, \tag{3.3}$$

where I_{PLC} is a constant base level of PLC activation in the cell and d_{PLC} is a deactivation rate. The term $I_{stimPLC}(t)$ represents the enhanced PLC activation rate due to stimulation by external factors, here, EGF. We propose a stimulation term of the form

$$I_{stimPLC}(t) = \begin{cases} I_{stim} \cdot EGF & \text{when stimulated by EGF,} \\ 0 & \text{otherwise.} \end{cases},$$

where stimulation by EGF is represented by a Heaviside (step) function $EGF(t) = H(t - t_{on}) - H(t - t_{off})$. In the absence of external stimulation, $I_{stimPLC} = 0$, and PLC activity is at its resting level

$$PLC_{rest} = \frac{I_{PLC}}{d_{PLC}}.$$

We normalize equation 3.3 in terms of this resting value, $PLC(t) = PLC_{rest} \cdot plc(t)$, where $plc(t)$ is a dimensionless variable. Equation 3.3 becomes

$$\frac{dplc}{dt} = d_{PLC}(\tilde{I}_{stimPLC}(t) + 1 - plc), \tag{3.4}$$

where

$$\tilde{I}_{stimPLC}(t) = \frac{I_{stimPLC}(t)}{I_{PLC}},$$

is a ratio of elevated activation rate to basal activation. These parameters can be fit well using data from Mouneimne (2004) [24], outlined in Section 3.4.1.

2. **Dynamics of PIP_2:** Similarly, we assume that a basal membrane concentration of the phosphoinositide PIP_2 exists in a resting cell. PIP_2 is known to bind and inactivate cofilin molecules at the membrane. Furthermore, the release of this pool of PIP_2-bound cofilin upon stimulation of the cell is proposed as the source of enhanced cofilin activity [33].

We assume PIP_2 to be in equilibrium under rest conditions of the cell, and that resting rates of production and decay are low [33]. Upon EGF stimulation, increased PLC activity catalyzes increased hydrolysis of PIP_2 at the membrane [24, 33]. We represent this phenomenon by introducing a PLC-mediated hydrolysis rate d_{hyd}, in effect when PLC activity is elevated above rest levels. At this point, we consider only the effect of PLC-mediated enhanced PIP_2 hydrolysis. We currently neglect other dynamics of the phosphoinositide pathway for simplicity.

We propose the following equation of PIP_2 dynamics

$$\frac{dP_2}{dt} = \underbrace{I_{P_2} - d_{P2}P_2}_{basal\ rates} - \underbrace{\left(\frac{d_{hyd}}{PLC_{rest}}\right)(PLC - PLC_{rest})P_2}_{PLC-mediated\ hydrolysis}. \tag{3.5}$$

At rest, Equation 3.5 leads to

$$P_{2,rest} = \frac{I_{P2}}{d_{P2}}.$$

Normalizing P_2 in Equation 3.5 by its resting steady state level, $P_2(t) = P_{2,rest} \cdot p_2(t)$, where $p_2(t)$ is dimensionless, obtains the scaled equation

$$\frac{dp_2}{dt} = d_{P2}(1 - p_2 - \tilde{d}_{hyd}(plc - 1)p_2), \tag{3.6}$$

where

$$\tilde{d}_{hyd} = \frac{d_{hyd}}{d_{P2}}.$$

Similar to $\tilde{I}_{stimPLC}$, the parameter $\tilde{d}_{hyd}$ is a dimensionless ratio of stimulated and resting rates, in this case (PLC-mediated hydrolysis of PIP_2)/(basal decay rates). The estimation of PIP_2 parameters (Section 3.4.1) relies on the rough PIP_2 temporal data shown in Figure 1.2 (from van Rheenen (2007) [33]).

3. **Dynamics of cofilin bound to PIP_2 at the membrane:** Experimental work has verified that a population of cofilin molecules is bound to PIP_2 at the membrane of a resting cell [14, 33]. We assume that cofilin binds to PIP_2 in a 1:1 binding ratio, and is thus released from the membrane upon EGF stimulation at the same rate as PIP_2 hydrolysis.

We assume that membrane-bound cofilin, C_2, is formed by dephosphorylation of inactive phospho-cofilin, C_P. For now, we assume C_2 recovers at a constant dephosphorylation rate and binds to PIP_2 at the membrane with mass-action kinetics.

The equation for membrane-bound cofilin is

$$\frac{dC_2}{dt} = \underbrace{\left(\frac{k_{P2}}{P_{2,rest}}\right) P_2 C_P}_{phospho-cofilin\ binds\ PIP2} - \underbrace{d_{C2} C_2}_{basal\ unbinding} - \underbrace{\left(\frac{d_{hyd}}{PLC_{rest}}\right)(PLC - PLC_{rest}) C_2}_{Loss\ via\ PIP2\ hydrolysis}. \tag{3.7}$$

The first term represents a simplified PIP_2 binding rate of phosphorylated cofilin that is stripped of its phosphate group.

Here we approximate the re-binding of cofilin to the membrane, neglecting the distinct processes of cofilin dephosphorylation and PIP_2 binding. The recycling process rebuilds membrane-associated cofilin slowly as shown in the time profiles of phosphorylated cofilin in Fig 2 of Song (2006) [31], and the PIP_2 recovery in Figure 1.2 of this theisis (from van Rheenen (2007) [33]).

Normalizing the cofilin variables by the average concentration of cofilin in the cell $C_i(t) = C_{tot} \cdot c_i(t)$, and substituting the normalized PLC and PIP_2 variables, plc and p_2, the fraction of cellular cofilin that is bound to PIP_2 is described by

$$\frac{dc_2}{dt} = k_{P2} p_2 c_p - d_{C2} c_2 - d_{hyd}(plc - 1) c_2. \tag{3.8}$$

4. **Dynamics of active cofilin:** We assume that the cofilin released from PIP_2 is in a free, unligated state. We consider this uninhibited state to be active, C_A, as it is ready to bind actin filaments. We assume that active cofilin is released at the membrane from the PIP_2-bound (C_2) pool. Active cofilin can be phosphorylated (to C_P) by LIM-Kinase, and consequently deactivated. We also assume active cofilin to be in equilibrium with actin filaments in a resting cell, with on and off rates proportional to concentrations in respective pools.

The resulting equation for active cofilin is

$$\frac{dC_A}{dt} = d_{C2}C_2 + \underbrace{k_{off}C_F - (k_{on}F)C_A}_{off-on\ actin\ filaments} - \underbrace{k_pC_A}_{phosphorylation} + \left(\frac{d_{hyd}}{PLC_{rest}}\right)(PLC - PLC_{rest})C_2, \tag{3.9}$$

where $(k_{on}F)$, and k_{off} are the filament binding and unbinding rate constants, k_p is the rate constant of phosphorylation by LIMK, d_{C2} is the decay of PIP_2-bound cofilin, and d_{hyd} is the rate constant of PLC-mediated PIP_2 hydrolysis described previously, all in units s^{-1}.

Scaling by the average concentration of cellular cofilin, so $C_A(t) = C_{tot} \cdot c_a(t)$, results in the equation for the active cofilin fraction, in dimensionless form

$$\frac{dc_a}{dt} = d_{C2}c_2 + k_{off}c_f - (k_{on}F)c_a - k_pc_a + d_{hyd}(plc - 1)c_2. \tag{3.10}$$

5. **Dynamics of filament-bound cofilin:** Cofilin that is bound to F-actin makes up the pool C_F. We assume that severing of filaments occurs in a resting cell at a basal rate proportional to the rest concentration of filament-bound cofilin, with rate constant k_{sev}. We assume loss of filament-bound cofilin is proportional to the concentration of bound cofilin.

We use a nonlinear unsaturated severing rate function $F_{sev}(C_F)$, as described in Section 2.5

$$F_{sev}(C_F) = k_{sev}C_{F,rest}\left(\frac{C_F}{C_{F,rest}}\right)^n,$$

where $n = 7$, and $k_{sev} << 1s^{-1}$ so that barbed end production by cofilin severing is low at rest conditions. We assume that following a severing event, the bound cofilin molecules are released from the filament in an actin-monomer-bound inactive form which must be recycled before rebinding to filaments.

The dynamics of the filament-bound cofilin compartment are described, at this stage by

$$\frac{dC_F}{dt} = (k_{on}F)C_A - k_{off}C_F - \underbrace{k_{sev}C_{F,rest}\left(\frac{C_F}{C_{F,rest}}\right)^n}_{nonlinear\ filament\ severing}. \tag{3.11}$$

Under these assumptions, the term $k_{sev}C_{F,rest}$ is the only source of inactive monomer-bound cofilin. The model expansion outlined in Chapter 4 investigates the possibility of active cofilin binding to G-actin monomers in the cytosol as another potential source of monomer-bound cofilin.

Normalizing C_F in Equation 3.11 by the average cofilin concentration in the cell, so $C_F(t) = C_{tot} \cdot c_f(t)$, leads to

$$\frac{dc_f}{dt} = (k_{on}F)c_a - k_{off}c_f - k_{sev}\phi_F\left(\frac{c_f}{\phi_F}\right)^n, \tag{3.12}$$

where

$$\phi_F = \frac{C_{F,rest}}{C_{tot}} = c_{f,rest}.$$

6. **Dynamics of G-actin monomer-bound cofilin:** After an actin filament severing event, cofilin is left bound to an actin monomer, termed C_M, as described in van Rheenen (2007) [33]. Cofilin in this form is inactive, unable to bind and sever actin again until it is recycled to the membrane. This requires an actin monomer-stripping and phosphorylation-dephosphorylation process. We use the approximation that monomer-bound cofilin transitions into the phosphorylated pool at a rate proportional to C_M concentration, with a rate constant equal to the phosphorylation rate of active cofilin, k_p.

The proposed equation is

$$\frac{dC_M}{dt} = \underbrace{k_{sev}C_{F,rest}\left(\frac{C_F}{C_{F,rest}}\right)^n}_{source} - \underbrace{k_pC_M}_{phosphorylation}, \tag{3.13}$$

with normalized form

$$\frac{dc_m}{dt} = k_{sev}\phi_F\left(\frac{c_f}{\phi_F}\right)^n - k_pc_m. \tag{3.14}$$

Here we neglect the monomer-stripping step of the recovery process for simplicity. Thus, we work under the assumption that the monomer is stripped and cofilin is phosphorylated in one step, whereby phosphorylation is the rate-determining step of the process. We examine the implications of this assumption in Chapter 4.

7. **Dynamics of phosphorylated cofilin:** Cofilin is inactivated in the cytosol by phosphorylation via LIM-Kinase. Cofilin in this C_P pool is inhibited from binding both PIP_2, and actin filaments. Phosphorylation of two different cofilin pools, active cofilin (C_A) and monomer-bound cofilin (C_M) are considered, assuming with the same rate k_p. Phosphorylated cofilin rebinds PIP_2 at the membrane via a dephosphorylation process which requires a stripping proteinase SSH or CIN [31, 32]. We assume here a (slow) dephosphorylation rate proportional to concentration of phospho-cofilin and mass action binding kinetics proportional to concentrations of phosphorylated cofilin and PIP_2.

The proposed equation governing dynamics of the phosphorylated cofilin pool is

$$\frac{dC_P}{dt} = k_p C_A + k_p C_M - \left(\frac{k_{P2}}{P_{2,rest}}\right) P_2 C_P, \tag{3.15}$$

with scaled form

$$\frac{dc_p}{dt} = k_p(c_a + c_m) - k_{P2} p_2 c_p. \tag{3.16}$$

8. **Dynamics of Barbed Ends:** Following the reduced model outlined in Chapter 2 and Section 2.5, we propose a barbed end equation where barbed end production in a stimulated cell is dependent on filament-bound cofilin C_F. Barbed end dynamics are governed by the equation

$$\frac{dB}{dt} = \underbrace{P_B - k_{cap} B}_{basal\ source-sink} + \underbrace{\alpha k_{sev} C_{F,rest} \left(\frac{C_F}{C_{F,rest}}\right)^n}_{cofilin-induced\ rate}, \tag{3.17}$$

where the rates P_B and $k_{sev} C_{F,rest}$ represent barbed end production in a resting cell, k_{cap} is the capping rate constant, n is the nonlinear severing factor and α is the estimated conversion factor between cofilin used and barbed ends created, and converts between units of cofilin concentration (μM) and barbed end density (number per μm^3).

Here we apply an assumption that the basal severing rate by filament-bound cofilin is negligible with respect to the production rate P_B, so that $\alpha k_{sev} C_{F,rest} << P_B$. Consequently, the resting barbed end concentration

$$B_{rest} = \frac{P_B + \alpha k_{sev} C_{F,rest}}{k_{cap}},$$

is approximated by

$$B_{rest} \approx \frac{P_B}{k_{cap}}.$$

We normalize the barbed end density by the approximate rest steady state and scale cofilin concentration by the average cofilin concentration in the cell to obtain

$$\frac{db}{dt} = A k_{sev} \phi_F \left(\frac{c_f}{\phi_F} \right)^n - k_{cap}(b-1), \tag{3.18}$$

where $\phi_F = c_{f,rest}$, and the conversion parameter α is combined with scaling factors in the parameter

$$A = \alpha \frac{C_{tot}}{B_{rest}},$$

as in Chapter 2. The approximation step described here must be verified with cofilin parameters and information from the literature, that is, whether the filament-severing rate is much lower than other basal rates of barbed end production, $\alpha k_{sev} C_{F,rest} < P_B$. The model simulation results using a non-approximated barbed end equation are outlined in Chapter 4.

3.3 Full Normalized Model

The assumptions and simplifications described in Section 3.2 allow us to propose a simple model framework for a closed, temporal model of the cofilin activity cycle. The collected equations for the full model are displayed in the Appendix.

The equations of the scaled model are:

$$\frac{dplc}{dt} = d_{PLC}(\tilde{I}_{stimPLC}(t) + 1 - plc), \tag{3.19}$$

$$\frac{dp_2}{dt} = d_{P2}(1 - p_2 - \tilde{d}_{hyd}(plc - 1)p_2), \tag{3.20}$$

$$\frac{dc_2}{dt} = k_{P2}p_2c_p - d_{C2}c_2 - d_{hyd}(plc - 1)c_2, \tag{3.21}$$

$$\frac{dc_a}{dt} = d_{C2}c_2 + k_{off}c_f - (k_{on}F)c_a - k_pc_a + d_{hyd}(plc - 1)c_2, \tag{3.22}$$

$$\frac{dc_f}{dt} = (k_{on}F)c_a - k_{off}c_f - k_{sev}\phi_F\left(\frac{c_f}{\phi_F}\right)^n, \tag{3.23}$$

$$\frac{dc_m}{dt} = k_{sev}\phi_F\left(\frac{c_f}{\phi_F}\right)^n - k_pc_m, \tag{3.24}$$

$$\frac{dc_p}{dt} = k_pc_a + k_pc_m - k_{P2}p_2c_p, \tag{3.25}$$

$$\frac{db}{dt} = k_{cap}(1 - b) + Ak_{sev}\phi_F\left(\frac{c_f}{\phi_F}\right)^n. \tag{3.26}$$

The dynamics of PLC and PIP_2, Equations 3.19 and 3.20 are decoupled from the rest of the system. The cofilin equations, 3.21-3.25 represent the closed cofilin activity cycle and are strongly coupled by interconversion terms. The solution of the barbed end equation, 3.26 is a system readout which is dependent on the profile of filament bound cofilin, $c_f(t)$, the solution of Equation 3.23 (recall that $\phi_F = c_{f,rest}$).

In the absence of a stimulus, the system has a basal steady state where PLC and PIP_2 are at their respective basal levels $plc = 1$ and $p_2 = 1$. Similarly, barbed end density is at its resting steady state, $b = 1$. The equations of cofilin concentrations, 3.21-3.25, are expressed as fractions of the average concentration of the cell, the respective steady state are given in Table 3.1.

If a stimulus is introduced, such that $\tilde{I}_{stimPLC}(t) = \tilde{I}_{stim} > 0$, a stimulated steady state exists where PLC activity is enhanced above resting levels, $plc > 1$. The elevated activity of

PLC induces a transient response in the cofilin cycle, which is known experimentally to increase filament-severing, and create a burst of barbed end density. To quantify this transient response with the above model, we require parameter estimates obtained from the experimental literature.

3.4 Model Parameter Analysis

The equations of the model represent a downstream cascade of effects initialized by PLC and PIP_2 dynamics at the cell membrane. The cofilin cycle returns to resting steady state on a slow time scale following EGF stimulation. This simplifies model analysis, as dynamics of PLC activity and PIP_2 can be fit to data independently of cofilin considerations. Cofilin transition rates can be examined based on PLC and PIP_2 results, model assumptions and available data about respective cofilin fractions.

3.4.1 PLC and PIP_2 Parameters

We first study the most upstream entity, PLC activity. In the right panel Figure 3.2, we reproduce the PLC activity profile subject to EGF stimulation shown in the left panel of the same figure (from Mouneimne et al (2004) [24]).

The model equation 3.4 can produce a good representation of experimental results, as shown in Figure 3.2. To obtain accurate time scale and relative proportions of stimulated and basal levels, we assign parameter values $d_{PLC} = 0.018s^{-1}$ and use scaled stimulation rates in the range $\tilde{I}_{stim}$ = 1.3-1.6, such that during stimulation, the scaled stimulated production of PLC activity is $I_{stimPLC}(t)$ = 1.3-1.6. In view of the reasonable agreement, we use the values

$$d_{PLC} = 0.018s^{-1}, \quad \tilde{I}_{stim} = 1.5.$$

The simple combined model consisting of Equations 3.19 and 3.20 facilitates the analysis of the decay rate of PIP_2, d_{P2}, and the nondimensional PLC-mediated PIP_2 hydrolysis rate, $\tilde{d}_{hyd}$. In combination, these determine the PIP_2 reduction due to hydrolysis as well as the recovery time back to basal levels.

From van Rheenen et al (2007), PIP_2 decreases to a minimum of 40-60% of its basal level

upon EGF stimulation [33]. Figure 1 A in that paper, shown here in the left panel of Figure 3.3, shows PIP_2 levels recover half of the lost concentration on a time scale of approximately $360s$. This suggests a decay rate $d_{P2} \approx \ln(2)/(360) \approx 0.0018s^{-1}$. Comparison between the simulations in the right panel of Figure 3.3 with the PIP_2 data in Figure 1.2, suggests a reasonable value of $\tilde{d}_{hyd}$ in the range of 10-20. This means that the PLC-dependent hydrolysis of PIP_2 is 10-20 times greater than resting background decay rate of PIP_2 due to other processes. For model simulations, we adopt the parameter settings

$$d_{P2} = 0.0018s^{-1}, \quad \tilde{d}_{hyd} = 20.$$

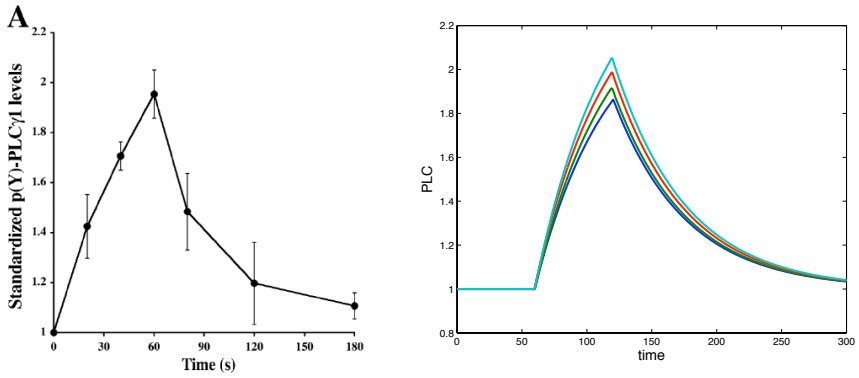

Figure 3.2: Left: Dynamics of PLC from Figure 2 A of Mouneimne (2004) [24]. Reprinted with permission from G Mouneimne: Spatial and temporal control of cofilin activity is required for directional sensing during chemotaxis. *Current Biology* 16(22):2193-205 (2006).
Right: Dynamics of PLC resulting from Eqn. 3.19, with $d_{PLC} = 0.018s^{-1}$ and $\tilde{I}_{stim} = 1.3$ (blue), $\tilde{I}_{stim} = 1.4$ (green), $\tilde{I}_{stim} = 1.5$, (red), and $\tilde{I}_{stim} = 1.6$ (cyan). We notice that the model is robust in these parameter settings. $\tilde{I}_{stim}$ determines maximum peak of PLC activity, $d_{PLC} = 0.018s^{-1}$ gives a good fit to experimental results.

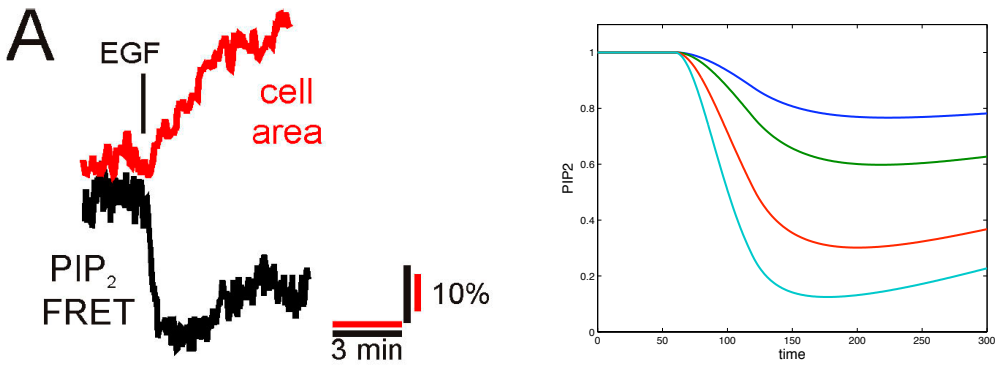

Figure 3.3: Dynamics of PIP_2 resulting from equation 3.20 for various values of the parameters. Right: Dynamics of PIP_2 from Figure 1 A of van Rheennen (2007) [33]. Reprinted with permission from J van Rheenen EGF-induced PIP_2 hydrolysis releases and activates cofilin locally in carcinoma cells. *Journal of Cell Biology* 179(6):1247-59 (2007).
Right: PIP_2 profiles for fixed $d_{P2} = 0.018s^{-1}$ and varying PLC-dependent hydrolysis strengths, $\tilde{d}_{hyd} = 2$ (blue), $\tilde{d}_{hyd} = 4$ (green), $\tilde{d}_{hyd} = 10$ (red), and $\tilde{d}_{hyd} = 20$ (cyan). The parameter $d_{P2} = 0.018s^{-1}$ was chosen to give our estimated best fit of PIP_2 recovery. We can compare these curves to the experimental data by van Rheenen's Figure 1A to select parameters for our (rough) approximation of PIP_2 dynamics

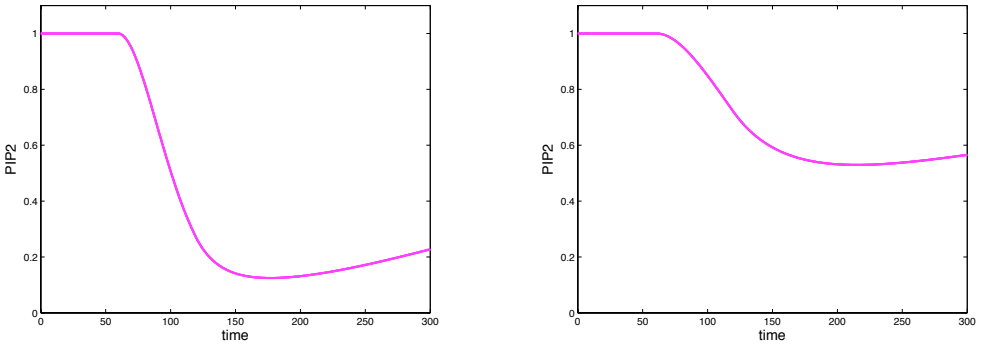

Figure 3.4: Model simulations of PIP_2 dynamics with $d_{P2} = 0.018s^{-1}$, and Left: $\tilde{d}_{hyd} = 20$ so that PIP_2 is almost completely reduced in the periphery, as per discussions with J. Condeelis, and Right: $\tilde{d}_{hyd} = 5$, a fit to the van Rheenen data.

3.4.2 Cofilin Data Review

We can use the resting state concentrations, together with data from the literature to satisfy the at rest steady state equations and solve for unknown model parameter values. In this section, I first outline available time series information, then compare with the parameter constraints imposed by the model.

We interpret Figure 6 A of van Rheenen (2007) as an exponential fit of cofilin residence time, or decay, bound to either PIP_2 (recovery $t_{c2} = 3.7s$) or actin filaments (recovery $t_{cf} = 26s$) [33]. We recognize that under a linear model, these recovery times represent the half-life of the respective cofilin binding, such that the decay rate of C_2 is given by

$$d_{c2} = \frac{ln(2)}{t_{c2}} \approx 0.19s^{-1}. \tag{3.27}$$

We can estimate the loss of filament-bound cofilin, which under our model occurs by the sum of rates k_{off} and k_{sev}, both linear at rest

$$d_{cf} = k_{off} + k_{sev} = \frac{ln(2)}{t_{cf}} \approx 0.027s^{-1}. \tag{3.28}$$

We expect severing events to be rare in a resting cell, as barbed end production is tightly regulated and severing occurs primarily as stochastic fluctuations of the system. This implies that the off-rate, k_{off}, of cofilin being released from actin filaments without causing a severing event should be significantly higher that the severing parameter k_{sev}. This information is consistent with our assumption $k_{off>k_{sev}}$ together with *in vitro* filament severing rates given in the literature [1, 2] where

$$k_{sev} \approx 0.010\text{-}0.012s^{-1}.$$

If we interpret Figure 6 B of van Rheenen (2007) as the fit of a linear combination of the C_2 and C_F exponential decay equations, then

$$y = A_1 exp(-d_{c2}t) + A_2 exp(-d_{cf}t).$$

Using this method, the relative ratios of PIP_2-bound cofilin and filament-bound cofilin can be obtained for both a resting and stimulated cell. We obtain the at rest ratio from this figure, implemented as initial conditions in our model,

$$\frac{C_{2,rest}}{C_{F,rest}} = \frac{0.85}{0.15}.$$

This ratio decreases upon stimulation with EGF to

$$\frac{C_{2,stim}}{C_{F,stim}} = \frac{0.38}{0.62},$$

which is important for time profile fitting of our model simulations. Furthermore, Figure 2 in van Rheenen (2007) shows an observed 2-fold increase of filament-bound cofilin C_F upon stimulation with EGF.

Figure 2 of Song et al. (2006) [31], exhibits the time profile of phosphorylated cofilin before and after stimulation of the cell with EGF. The resting level is identified as $C_{P,rest} = 0.18(\pm 4) \cdot C_{tot}$, and stimulated level, which we take to be the maximum of the phosphorylated cofilin pool is $C_{P,max} = 0.38(\pm 6) \cdot C_{tot}$. Further time profiles of phospho-cofilin can be used to fit model simulations [31], but this is beyond the scope of this thesis. We use compare the experimental data of a stimulated cell to model simulations, shown in Section 4.8, and discuss conclusions in Chapter 5.

3.4.3 Cofilin Model Parameter Analysis

Here we outline the analysis of model assumptions and equations to combine with available cofilin data from Section 3.4.2 to gain information about unknown model parameters.

The information given in Song et. al (2006), [31], implies the rest fraction of phosphorylated cofilin in the cell to be

$$c_{p,rest} = 0.20.$$

Through analysis of Figure 6 of van Rheenen (2007) [33], the ratio of cofilin bound to F-actin

and PIP_2 at the periphery of the cell is identified as

$$\frac{c_{f,rest}}{c_{2,rest}} \approx \frac{0.15}{0.85},$$

which gives $c_{2,rest} \approx 5.8 \cdot c_{f,rest}$. From personal communication with J. Condeelis, we estimate the fraction of PIP_2-bound cofilin at rest as $c_{2,rest} \approx 0.10$. This supports resting level fractions of filament-bound, and PIP_2-bound cofilin to be approximately

$$\begin{aligned} c_{f,rest} &= 0.02, \\ c_{2,rest} &= 0.10. \end{aligned}$$

The conservation assumption Equation 3.2 also implies that, at rest, the normalized cofilin pools sum up to 1

$$c_{2,rest} + c_{a,rest} + c_{f,rest} + c_{m,rest} + c_{p,rest} = 1. \tag{3.29}$$

Thus the sum of at rest steady state fractions of active and monomer-bound cofilin is approximately

$$\begin{aligned} c_{a,rest} + c_{m,rest} &= 1 - c_{2,rest} - c_{f,rest} - c_{p,rest} \\ &= 1 - 0.10 - 0.02 - 0.20 \\ &= 0.68. \end{aligned} \tag{3.30}$$

We first identify steady state relationships between resting cofilin pool levels. We set derivatives of Equations 3.21-3.25 to zero, and use the assumption $k_{sev} << 1s^{-1}$. From equation 3.21, parameters must satisfy the relationship

$$c_{2,rest} = \frac{k_{P2} \cdot p_{2,rest}}{d_{C2}} \cdot c_{p,rest}, \tag{3.31}$$

where $c_{i,rest}$ is the scaled cofilin level and $p_{2,rest} = 1$ is scaled PIP_2 level in the resting cell.

Equation 3.31, together with the rest levels data of PIP_2-bound and phosphorylated cofilin,

provides a relationship between the dephosphorylation rate of the model k_{P2} and the decay rate of PIP_2 cofilin d_{C2}. We have

$$k_{P2} = \frac{c_{2,rest}}{p_{2,rest} \cdot c_{p,rest}} \cdot d_{C2} = \frac{0.10}{1 \cdot 0.20} \cdot d_{C2},$$

so that

$$k_{P2} = 0.5 \cdot d_{C2}.$$

Since PIP_2-bound cofilin decays as PIP_2 decays at the membrane, we assume $d_{C2} = d_{P2}$. The PIP_2 decay rate constant, d_{P2} approximated in Section 3.4.1. We then set parameter values

$$d_{C2} = 0.002s^{-1}, \qquad k_{P2} = 0.001s^{-1}.$$

Furthermore, from equation 3.25

$$c_{p,rest} = \frac{k_p}{k_{P2}} \cdot (c_{a,rest} + c_{m,rest}). \tag{3.32}$$

From above, the rest fraction of phospho-cofilin is $c_{p,rest} = 0.20$, and from Equation 3.30 $c_{a,rest} + c_{m,rest} = 0.68$. This gives the relation

$$\frac{0.68}{0.20} = \frac{k_{P2}}{k_p},$$

and

$$k_{P2} = 3.40 \cdot k_p.$$

The phosphorylation rate can be approximated as

$$k_p = 2.94 \cdot 10^{-4} s^{-1}.$$

The steady state equation of monomer-bound cofilin, Equation 3.24 can be simplified, since

$\phi_F = C_{F,rest}/C_{tot} = c_{f,rest}$. This identifies the relationship

$$c_{m,rest} = \frac{k_{sev}}{k_p} \cdot c_{f,rest}. \tag{3.33}$$

Notice that the ratio between monomer-bound and filament-bound cofilin at resting conditions is determined here by the ratio between basal severing and phosphorylation rates. This implies

$$\frac{c_{m,rest}}{c_{f,rest}} = \frac{k_{sev}}{k_p}. \tag{3.34}$$

We identify this parameter k_{sev}, (for which there are estimates only from *in vitro* work and other modeling efforts [1, 6]), as a free parameter to be tested by model simulations. It is identified by the constraints of Equation 3.34 once the rest steady state level of monomer-bound cofilin, $c_{m,rest}$ is assigned.

From discussion with J. Condeelis, we work under the assumption that the fraction of active cofilin is very small at any time t. Condeelis predicts this cofilin fraction to be near zero in a resting cell, therefore, we estimate the rest level of active cofilin pool of cofilin as $c_{a,rest} \approx 0.01$. By conservation, Equation 3.30, this gives $c_{m,rest} = 0.67$. This identifies the severing model parameter, since to satisfy Equation 3.34, we have

$$k_{sev} = \frac{0.67}{0.02} \cdot \ k_p,$$

so

$$k_{sev} = 0.0099 s^{-1}.$$

In line with the conservation equation 3.30,

$$\begin{aligned} c_{m,rest} &= 0.67, \\ c_{a,rest} &= 0.01. \end{aligned}$$

The cofilin equations 3.22 and 3.23 introduce two actin-binding parameters, k_{off} and simplified binding rate constant ($k_{on}F$). From Equation 3.28, and the linear decay of filament-bound

cofilin from Equation 3.23, we obtain the relationship between rate constants of loss of filament-bound cofilin

$$k_{off} = d_{cf} - k_{sev} = 0.027s^{-1} - 0.0099s^{-1}, \tag{3.35}$$

$$= 0.0171s^{-1} \tag{3.36}$$

based on previous assumptions. Thus the model assumptions satisfy experimental predictions that $k_{off} > k_{sev}$.

We can gain further information about parameters by using the relationship between steady states of Equations 3.10 and 3.12

$$c_{a,rest} = \frac{1}{k_p + (k_{on}F)} \cdot [d_{C2}c_{2,rest} + k_{off}c_{f,rest}], \tag{3.37}$$

and

$$c_{f,rest} \approx \frac{k_{on}F}{k_{off} + k_{sev}} \cdot c_{a,rest}. \tag{3.38}$$

Setting the relations for $c_{a,rest}$ equal to one another and simplifying obtains the relation

$$\frac{k_p k_{sev} + k_p k_{off} + (k_{on}F)k_{sev}}{(k_{on}F)d_{C2}} = \frac{c_{2,rest}}{c_{f,rest}},$$

which can be further simplified to be in terms previously identified parameter ratios

$$\frac{d_{C2}}{k_p} \cdot \frac{c_{2,rest}}{c_{f,rest}} - \frac{c_{m,rest}}{c_{f,rest}} = \frac{k_{sev} + k_{off}}{(k_{on}F)}. \tag{3.39}$$

From Equation 3.38, together with previous assumptions about resting concentrations and resulting parameter estimates, we find that the filament association and dissociation parameters must satisfy

$$6.80 \cdot 5.0 - 33.50 = \frac{k_{sev} + k_{off}}{(k_{on}F)} = \frac{c_{a,rest}}{c_{f,rest}}.$$

Here we have defined $c_{a,rest} = 0.01$, so

$$(k_{on}F) = 2 \cdot (k_{sev} + k_{off}).$$

Using experimental data from van Rheenen (2007) (Section 3.4.2), the filament binding rate is estimated as

$$(k_{on}F) = 2 \cdot \frac{ln(2)}{26} s^{-1} = 0.054 s^{-1}.$$

3.5 Summary of Model Equations and Parameters

We simulate the system of ODEs, Equations 3.19-3.26 using parameter values described in Section 3.4.3 and summarized in Table 3.2 and 3.3. The system is initialized at the respective rest steady states. The stimulus is introduced as an EGF step function turned on at $t = 60s$ and off at $t = 120s$, such that

$$\tilde{I}_{stimPLC}(t) = \tilde{I}_{stim}(\text{Heaviside}(t-60) - \text{Heaviside}(t-120)).$$

Cofilin Pool	Description	Resting Level	Source
C_2	PIP_2-bound cofilin	$0.10 \cdot C_{tot}$	van Rheenen 2007 [33]
C_A	active cofilin	$0.01 \cdot C_{tot}$	approximated in model
C_F	F-actin-bound cofilin	$0.02 \cdot C_{tot}$	van Rheenen 2007 [33]
C_M	G-actin-monomer-bound	$0.67 \cdot C_{tot}$	conservation assumption
C_P	phosphorylated cofilin	$0.20 \cdot C_{tot}$	Song 2006 [31]
C_{tot}	total cellular cofilin	$10\mu M$	Pollard 2000 [26]

Table 3.2: Definitions of the forms of cofilin modeled in this chapter with rest steady state concentrations

Parameter	Description	Value	Source
$\tilde{I}_{stim}$	scaled PLC activation rate	1.5	Mouneimne 2004 [24]
d_{PLC}	PLC decay rate	$0.018 s^{-1}$	Mouneimne 2004 [24]
d_{P2}	PIP_2 resting hydrolysis	$0.002 s^{-1}$	van Rheenen 2007 [33]
d_{hyd}	PLC-PIP_2 hydrolysis rate	$0.01 s^{-1}$	van Rheenen 2007 [33]
d_{C2}	PIP_2-cofilin decay rate	$0.002 s^{-1}$	assumption
k_{off}	Cofilin-F-actin off-rate	$0.0171 s^{-1}$	van Rheenen 2007 [33]
$k_{on}F$	Filament binding rate	$0.054 s^{-1}$	estimated by model
k_{sev}	Cofilin severing rate	$0.0099 s^{-1}$	estimated by model
k_p	Cofilin phosphorylation	$2.94 \cdot 10^{-4} s^{-1}$	estimated by model
k_{P2}	Dephosphorylation	$0.001 s^{-1}$	estimated by model
k_{cap}	Barbed end capping rate	$1 s^{-1}$	Dawes 2006 [9]
α	unit conversion factor	$600 \mu M^{-1} \mu m^{-3}$	Mogilner, LEK 2002 [21]
A	scaling factor	1000	Pollard 2000 [26]

Table 3.3: Parameter estimates for the well-mixed temporal model, Equations 3.19-3.26

3.6 Simulations of Well-Mixed Model

The following figures exhibit an example of simulation results of the well-mixed temporal cofilin system for proposed model assumptions and parameter estimates. We simulate two scenarios proposed by experiments. First, we use a PLC-hydrolysis parameter of $d_{hyd} = 0.01s^{-1}$ to produce a 60% reduction of PIP_2 levels, shown in the left panel of Figure 3.5. This represents the overall reduction of PIP_2 as given in van Rheenen (2007). The model simulations results are shown in Figures 3.6-3.8. Secondly, model simulation with $d_{hyd} = 0.04s^{-1}$ produces almost complete reduction of PIP_2, shown in the right panel of Figure 3.5. Motivated by discussions with J. Condeelis, this represents cellular activity in local regions near an EGF receptor. The results of model simulations are given in Figures 3.9-3.11.

The simulations of a 60% reduction in PIP_2 levels result in a similar reduction in the level of PIP_2-bound cofilin. The resulting barbed end density reaches a maximum increase of less than 5-fold over resting barbed end levels (Figure 3.8). This peak is enhanced by increasing the PIP_2 reduction, since this induces a much larger release of PIP_2-bound cofilin (Figure 3.10). This generates a barbed end peak of approximately 8-9 fold increase over resting levels (Figure 3.11). While these results reproduce the experimental increase in barbed ends, up to 10-12 fold, at a respectable level, both scenarios fail to generate the 2-fold increase in filament-bound cofilin shown in van Rheenen (2007).

In the next chapter, I outline our work to reformulate the well-mixed cell approximation. By working within a model framework which better represents the physical properties of a cell, we aim to analyze the assumptions made in this chapter and verify model results.

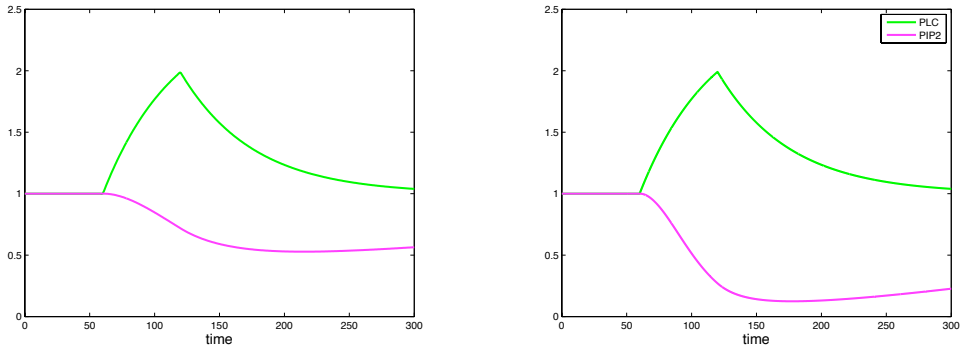

Figure 3.5: Simulation profiles of PLC (green) and PIP_2 (magenta) with parameter settings from Table 3.3 Left: Results for $d_{hyd} = 0.01s^{-1}$. Right: Results for $d_{hyd} = 0.04s^{-1}$.

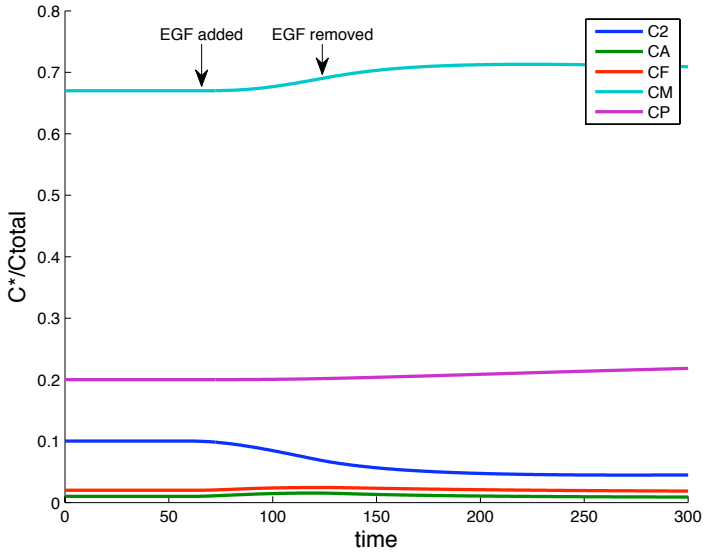

Figure 3.6: Cofilin time profiles as fractions of average cofilin concentration, for parameter settings outlined in Table 3.3.

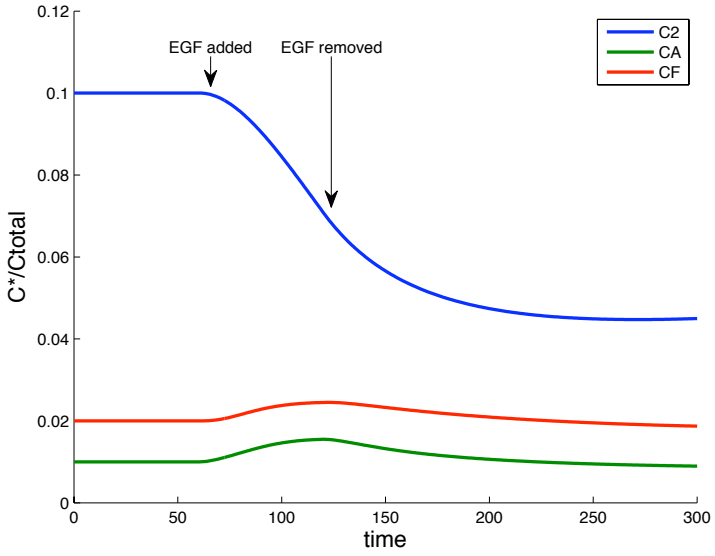

Figure 3.7: As in Figure 3.6, magnified to show a close up of low-level cofilin fraction profiles for parameter settings outlined in Table 3.3.

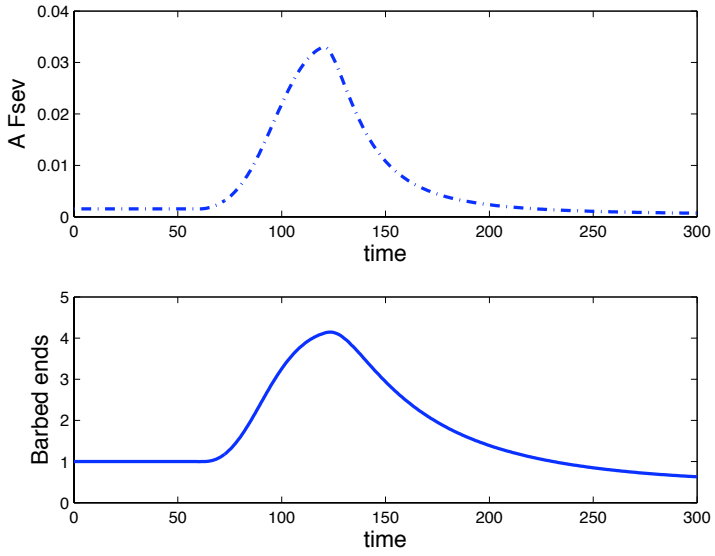

Figure 3.8: Rate of severing (top) and barbed end time profiles (bottom) produced by cofilin activity dynamics and using parameter settings outlined in Table 3.3. Notice small barbed end amplification of approximately 3-fold increase.

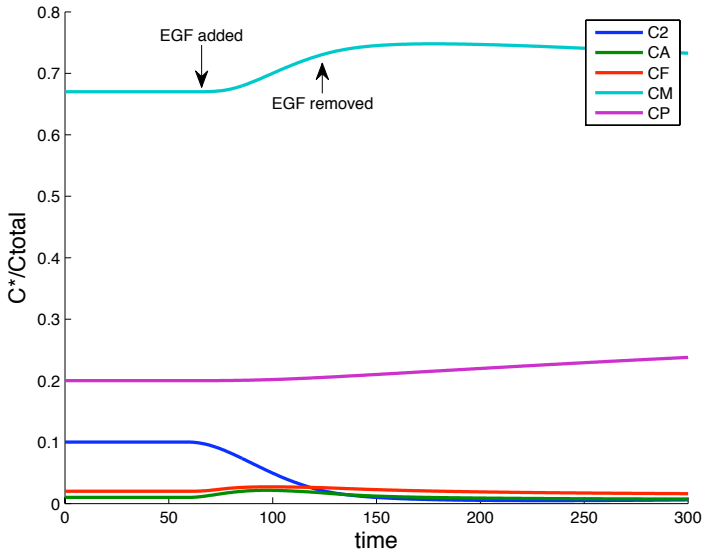

Figure 3.9: Cofilin time profiles as fractions of average cofilin concentration, for parameter settings outlined in Table 3.3 and $d_{hyd} = 0.04s^{-1}$.

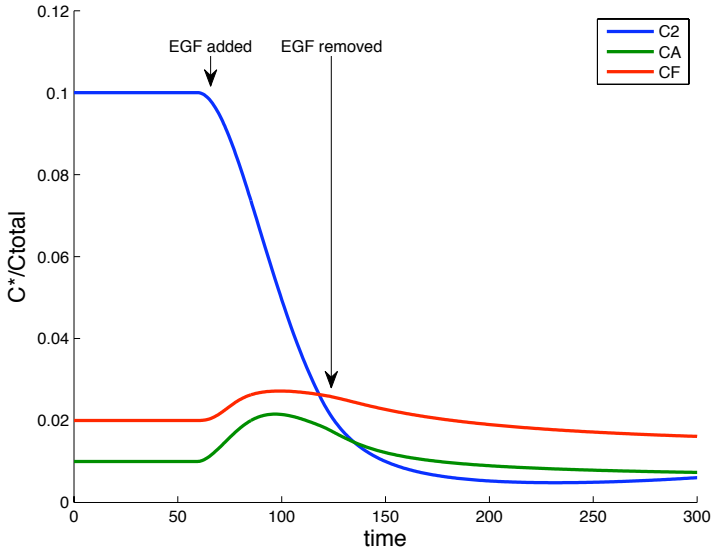

Figure 3.10: As in Figure 3.9, magnified to show a close up of low-level cofilin fraction profiles for parameter settings outlined in Table 3.3 and $d_{hyd} = 0.04s^{-1}$.

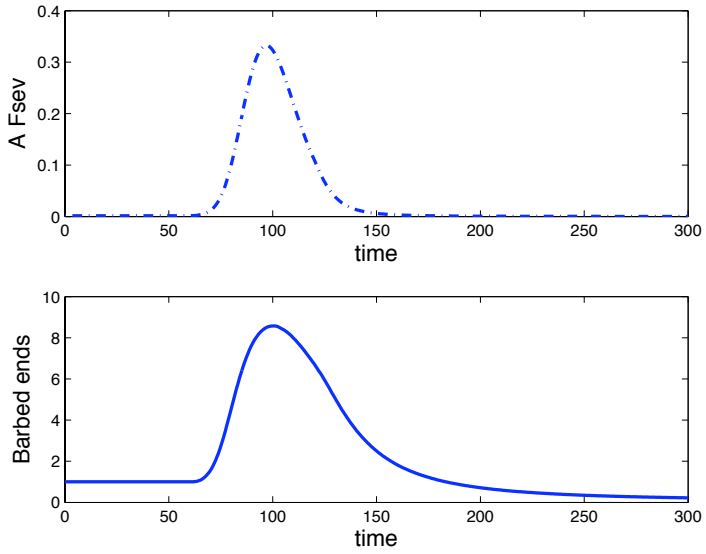

Figure 3.11: Rate of severing (top) and barbed end time profiles (bottom), shown as relative density over resting barbed end concentration, for parameter settings outlined in Table 3.3 and $d_{hyd} = 0.04s^{-1}$. Notice a barbed end amplification of over 8-fold with 60s of addition of EGF stimulus.

Chapter 4

Temporal Cofilin Compartmental Model

4.1 Introduction

In this chapter, I outline our examination of a compartmental model, challenging the well-mixed assumption of Chapter 3. We introduce two volume compartments, one to represent the small region at the cell edge and another to represent the large cellular interior. Compartmental considerations are supported by the desire to differentiate the cofilin forms identified to be bound at the cell edge by fluorescence-tagged membrane experiments versus those that diffuse freely in the cytosol [24, 33]. Cofilin bound to PIP_2 (C_2) has been shown to be stationary and membrane-associated [33]. Cofilin binding to F-actin is known experimentally to be confined to the periphery of the cell by inhibition of tropomyosin binding to filaments in the interior [12, 33]. These model revisions quantify relative local concentrations of cofilin in the periphery and cytosolic compartments by identifying the different volumes of the edge and interior compartments, which may be up to 1 or 2 orders of magnitude larger. This requires revision of the model equations to represent transition between compartments.

We also consider whether interactions previously neglected could be significant, so we include the reactivation of cofilin via direct dephosphorylation of C_P, re-binding of active cofilin C_A back onto PIP_2 at the membrane (into C_2 pool), and a new equilibrium relationship between active and monomer-bound cofilin. The revised definitions of cofilin pools in respective compartments are outlined in Table 4.1 and interactions between cofilin forms shown in the schematic, Figure 4.1.

This model version serves as the final step in the analysis of the temporal dynamics of the cofilin pathway before embarking on a spatio-temporal model. Here, we address all possible interactions between the identified cofilin forms with the goal of identifying the critical interactions to include in the spatial framework. A future one-dimensional (PDE) model should then simulate the distribution of cofilin as distance from the cell edge. Thus, the edge and interior compartments examined in this chapter will determine the boundary conditions of a radial model. This final temporal model also facilitates the verification of appropriate and necessary model assumptions to simplify future work.

Cofilin Pool	Description	Resting Level	Source
C_2^E	PIP_2-bound cofilin	$2.00 \cdot C_{tot}$	discussion
C_A^E	active cofilin in edge	$10^{-4} \cdot C_{tot}$	approximated in model
C_F^E	F-actin-bound cofilin	$0.40 \cdot C_{tot}$	van Rheenen 2007
C_M^E	G-actin-monomer-bound in edge	$0.67 \cdot C_{tot}$	conservation assumption
C_P^E	phosphorylated cofilin in edge	$0.20 \cdot C_{tot}$	Song 2006
C_A^I	active cofilin in interior	$10^{-4} \cdot C_{tot}$	approximated in model
C_M^I	G-actin-monomer-bound in interior	$0.67 \cdot C_{tot}$	conservation assumption
C_P^I	phosphorylated cofilin in interior	$0.20 \cdot C_{tot}$	Song 2006
C_{tot}	average cofilin concentration	$10\mu M$	Pollard 2000

Table 4.1: Cofilin forms in the edge and interior compartments, with rest concentrations defined relative to average cellular cofilin concentration.

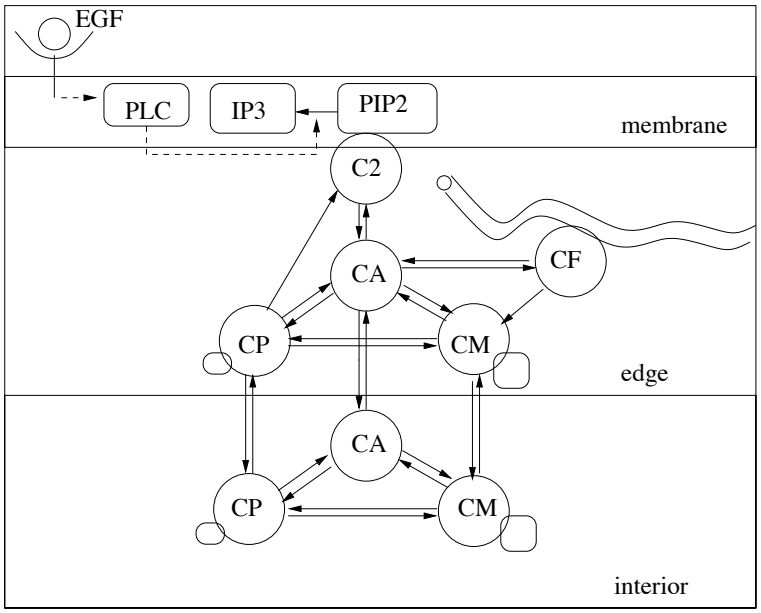

Figure 4.1: Schematic of proposed temporal compartmental model of cofilin pathway: Dynamics are separated into those at the edge of the cell, and interactions in the cytosol, or interior of the cell. At the membrane, EGF stimulation activates PLC, causing the membrane lipid PIP_2 to be hydrolyzed. This releases the cofilin from the membranous PIP_2-bound pool (C_2^E) to an active form (pool C_A^E) at the edge of the cell, from which it can attach to actin filaments (pool C_F^E), or bind to G-actin (C_M^E), phosporylated (to C_P^E), or rebind to PIP_2. Once the filament is severed, cofilin comes off, carrying an actin monomer (pool C_M^E) with it. Filament dynamics are assumed to occur near the membrane, in the edge compartment. Following a severing event, the G-actin-cofilin is stripped of its monomer, and phosphorylated by LIM kinase into the form C_P, so that it could reattach to PIP_2. The freely diffusing forms of cofilin diffuse between the edge and interior compartment, to C_A^I, C_M^I, C_P^I.

4.1.1 General Assumptions

- We will consider here only temporal dynamics, and thereby approximate the cell as a well-mixed system where cofilin molecules move freely between the cytosolic and peripheral compartments of the cell.

- Cellular cofilin is divided into several forms in the edge compartment (within 200 nm of the cell membrane) and in the interior compartment. Freely diffusing forms can transition between the two compartments, whereas cofilin molecules bound to PIP_2 at the membrane, or bound to filaments at the edge of the cell are confined to the edge compartment. We assume that the edge and interior compartments have fixed volumes, V^E and V^I respectively.

- The total amount of cofilin is conserved in the cell. We use the notation C_i^E and C_i^I to denote concentrations in micromolar units (μM) of cofilin in various forms. The total number of molecules of cofilin is given by the conservation statement

$$V^E \cdot (C_2^E + C_A^E + C_F^E + C_M^E + C_P^E) + V^I \cdot (C_A^I + C_M^I + C_P^I) = V_{tot} \cdot C_{tot} = (V^E + V^I) \cdot C_{tot}, \quad (4.1)$$

  where V^E, V^I are volumes of compartments, usually in μm^3, C_{tot} is the total average cofilin concentration in the cell ($10\mu M$), and the cofilin forms, C_i, are as defined in Table 4.1.

- Actin filament density is constant and abundant within the domain. We consider an actin binding rate dependent only on available cofilin, and assume filament severing to be independent of filament density for now.

- Barbed end dynamics are governed by equations proposed in earlier works and do not feed back on their own production. We assume that active barbed ends observed at 60s following stimulation with EGF are due to amplification of cofilin severing.

4.2 Model Details

Motivated by experimental conclusions, we define the edge compartment as the region within $200n$m of the cell membrane, and the interior compartment as the remaining fraction of the cell [33]. This implies a large difference in compartmental volumes, $V^I >> V^E$, confirmed by calculations outlined in the Appendix. Since some cofilin forms, C_2 and C_F exist only at the edge of the cell, whereas the other cofilin forms, C_A, C_M, and C_P are present at both the edge, and in the interior of the cell, we must consider the effective local densities of each cofilin fraction in the given compartment. We will denote relative local cofilin concentrations of respective forms as C_i^E in the edge compartment, and C_i^I in the interior. For example, monomer-bound cofilin concentration in the edge compartment is described by

$$C_i^E = \frac{\text{molar quantity of monomer-bound cofilin in edge}}{\text{volume of edge compartment}}.$$

We ensure that balance equations are written in terms of conservation of mass or of numbers of molecules. When compartment volumes differ, as in the case we describe here, this introduces some correction factors from dilution effects. To avoid confusion about relative local concentrations, we outline several different notations here. These all convey the same message, conservation of total cofilin, Equation 4.1. The quantity $V_{tot} \cdot C_{tot}$ has units $\mu\text{m}^3 \cdot \mu M$ since these are common units of measure.. Converting this quantity into number of molecules of cofilin requires a conversion factor η, described in the Appendix. The total number of cofilin molecules in the cell is given by

$$\#\text{molecules} = V_{tot} \cdot C_{tot} \cdot \eta,$$

where $\eta = 600$ molecules $\mu M^{-1}\mu\text{m}^{-3}$, since 1μM ≈ 600 molecules per μm^3, details of this calculation are outlined in the Appendix.

The available data that describes the resting cofilin concentrations in a cell is given as the proportion of total cofilin in the cell. We take these to be proportions of the total molecular content (as in fluorescence data). We use the average total cellular cofilin concentration of $10\mu M$ [26]. This allows us to calculate the total molecular content in our model cell approximation,

after choosing a volume estimate.

We can nondimensionalize Equation 4.1 by dividing by $V_{tot} \cdot C_{tot}$, obtaining the relationship

$$\frac{V^E}{V_{tot}}\left(\frac{C_2^E}{C_{tot}} + \frac{C_A^E}{C_{tot}} + \frac{C_F^E}{C_{tot}} + \frac{C_M^E}{C_{tot}} + \frac{C_P^E}{C_{tot}}\right) + \frac{V^I}{V_{tot}}\left(\frac{C_A^I}{C_{tot}} + \frac{C_M^I}{C_{tot}} + \frac{C_P^I}{C_{tot}}\right) = 1.$$

We define compartment volumes by total volume of the cell, and relative cofilin concentrations scaled by average cofilin concentration C_{tot}, defining

$$v^E = \frac{V^E}{V_{tot}}, \quad v^I = \frac{V^I}{V_{tot}}, \quad c_i = \frac{C_i}{C_{tot}},$$

This leads to the the nondimensional conservation equation

$$v^E \cdot (c_2^E + c_a^E + c_f^E + c_m^E + c_p^E) + v^I \cdot (c_a^I + c_m^I + c_p^I) = 1. \tag{4.2}$$

Finally, if we combine relative local concentrations with their respective volume fraction, such that

$$\tilde{c}_i^E = v^E \cdot c_i^E, \quad \tilde{c}_i^I = v^I \cdot c_i^I,$$

the conservation equation can be expressed as

$$(\tilde{c}_2^E + \tilde{c}_a^E + \tilde{c}_f^E + \tilde{c}_m^E + \tilde{c}_p^E) + (\tilde{c}_a^I + \tilde{c}_m^I + \tilde{c}_p^I) = 1.$$

Notice that the $\tilde{c}_i$ expression represents the fraction of total molecular cofilin in each respective form.

These modifications in methodology and model development introduce several new aspects to the model. First, available data gives estimates of resting cofilin fractions of respective forms [24, 31, 33]. We take these to be proportional to the average cofilin concentration in the cell. The fractions which exist in strictly the edge compartment must be scaled to obtain the relative local concentrations of each cofilin form. For example, if C_i, in units of μM, is the average cellular concentration of cofilin in form i, we can convert this to the relative local concentration in the edge compartment using the relationship

$$C_i^E = \frac{V_{tot}}{V^E} \cdot C_i.$$

Based on the exchange between compartments, we must now incorporate 3 additional ODEs in the system to describe the dynamics of C_A^I, C_M^I and C_P^I in the interior. The rate of change of each respective cofilin form in each compartment is described qualitatively by

$$\frac{d}{dt}[\text{molecules of form } i \text{ in compartment}] = \text{rate of exchange} + \text{source terms} - \text{loss terms}.$$

Currently, we assume that exchange between compartments follows simple diffusion. Transitions between compartments of each respective cofilin form occur at a rate proportional to the concentration difference. We utilize known cofilin diffusion coefficient ($D \approx 10\mu\text{m}^2 s^{-1}$) [26] to give the rate of molecular exchange and use a width parameter of the cell ($\omega = 0.2\mu\text{m}$) [21]. These parameters scale the compartmental transition terms and match units in Equations 4.3 and 4.4 The rate of change of cofilin in given forms satisfies

$$\frac{d(V^E C_i^E)}{dt} = \omega D[C_i^I - C_i^E] + \text{source terms} - \text{loss terms}, \tag{4.3}$$

$$\frac{d(V^I C_i^I)}{dt} = -\omega D[C_i^I - C_i^E] + \text{source terms} - \text{loss terms}. \tag{4.4}$$

The considerations of compartmental volumes and transitions affect only the diffusing forms that exchange between the edge and interior, not C_2 or C_F. We assume a constant diffusion coefficient for all forms of cofilin, though the coefficient describing diffusion of C_M may be slightly lower due to the larger structural size of the complex.

We also take into account several interactions neglected in previous modelling efforts. These include equilibrium binding of G-actin on/off active cofilin ($C_A \leftrightarrow C_M$), rebinding of active cofilin to PIP_2 at the membrane, and dephosphorylation of phospho-cofilin at locations other than the membrane. These interactions are included in the full model schematic shown in Figure 4.1. The addition of these interactions in the absence of further experimental data will require extensive simplifying model assumptions. However, we hope that the process will facilitate some insight into the importance of each respective interaction effect.

4.3 Model Equations

For the most part, equations will closely follow their forms in Equations 3.19-3.26. However, in this version, we expand the model to incorporate a more complete collection of potential cellular interactions.

We keep the same assumptions and equations for PLC and PIP_2, since these system components are not involved in the conservation equation. We proceed with the scaled equations as experimental data is commonly given in a normalized form as fold increases over resting levels.

I outline here the revised model equations for PIP_2-bound cofilin, C_2^E, and both edge and interior forms of active cofilin, C_A^E and C_A^I, where new terms are expressed in red font. The Equations 3.23-3.25 are revised in a similar manner to include new terms from Figure 4.1 and exchange between compartments.

1. **Dynamics of cofilin bound to PIP_2 at the membrane:** Since PIP_2 is a membrane-associated lipid, cofilin bound to PIP_2 is assumed to exist only in the membrane compartment. We quantify the cofilin bound to the membrane at any time t, as $\#\text{moles}C_2^E = V^E \cdot C_2^E$. The equation for membrane-bound cofilin dynamics is given by

$$\frac{d(V^E C_2^E)}{dt} = \underbrace{\left(\frac{k_{Pp2}}{P_{2,rest}}\right) P_2 V^E C_P^E}_{phospho-cofilin\ binds\ PIP2} + \underbrace{\left(\frac{k_{Ap2}}{P_{2,rest}}\right) P_2 V^E C_A^E}_{active\ cofilin\ binds\ PIP2} - \underbrace{d_{C2} V^E C_2^E}_{basal\ unbinding} - \underbrace{\left(\frac{d_{hyd}}{PLC_{rest}}\right)(PLC - PLC_{rest}) V^E C_2^E}_{Loss\ when\ PIP2\ hydrolyzed}, \quad (4.5)$$

   where terms are as previously with the addition of PIP_2-binding rates from phosphorylated and active cofilin forms, k_{Pp2} and k_{Ap2}, respectively. We then normalize the molecular level of PIP_2-bound cofilin by the total amount of cofilin in the cell to obtain fractions of total cellular cofilin,

$$v^E \cdot c_i^E = \frac{V^E}{V_{tot}} \cdot \frac{C_i^E}{C_{tot}}. \quad (4.6)$$

   Since fractioned edge compartment volume, $v^E = V^E/V_{tot}$, is assumed to be approximately constant in time, and appears in all terms here, we can divide it from both sides of

Equation 4.5. Using normalized PLC and PIP_2 variables, ($PLC(t) = PLC_{rest} \cdot plc(t)$), the nondimensional concentration of PIP_2-bound cofilin ($C_2(t) = C_{tot} \cdot c_2$) is

$$\frac{dc_2^E}{dt} = k_{Pp2}p_2c_p^E + k_{Ap2}p_2c_a^E - d_{C2}c_2^E - d_{hyd}(plc-1)c_2^E. \tag{4.7}$$

2. **Dynamics of active cofilin at the periphery:** Cofilin liberated from the membrane compartment is released into the edge compartment of the cell. We consider this cofilin form to be active (pool C_A^E), as it can bind to available and uninhibited actin filaments.

Active cofilin diffuses between the edge and interior compartments of the cell, at a rate proportional to its concentration difference. Here we assume G-actin monomers with respective on and off rates proportional to concentrations in respective pools. Expanding on assumptions of previous models, here we consider the reactivation of cofilin by dephosphorylation (from C_P) or loss of the actin monomer (from C_M). These considerations were motivated by conversations with J. Condeelis, and work shown in Mogilner, Keshet (2002) [21] respectively. The revised equation of active cofilin is

$$\begin{aligned}\frac{dV^EC_A^E}{dt} = &\underbrace{\omega D\left[C_A^I - C_A^E\right]}_{diffusion} + d_{C2}V^EC_2^E + k_{off}V^EC_F^E - (k_{on}F)V^EC_A^E - k_pV^EC_A^E \\ &+ \underbrace{k_{dp}V^EC_P^E}_{dephosphorylation} + \underbrace{k_{ma}V^EC_M^E - k_{am}V^EC_A^E}_{off-on-G-actin-monomer} - \underbrace{\left(\frac{k_{Ap2}}{P_{2,rest}}\right)P_2V^EC_A^E}_{active\ cofilin\ binds\ PIP2} \\ &+ \left(\frac{d_{hyd}}{PLC_{rest}}\right)(PLC - PLC_{rest})V^EC_2^E, \end{aligned} \tag{4.8}$$

where d_{C2}, $k_{on}F$, and k_{off}, k_p, and d_{hyd} are defined as before (in s^{-1}). The constants ω (μm) and D ($\mu m^2 s^{-1}$) are the cell width and diffusion parameters described previously, k_{am} and k_{ma} are G-actin-monomer binding and un-binding rates, and k_{dp} is the rate of dephosphorylation via various cellular phosphatases (s^{-1}).

We scale the equation for active cofilin dynamics as in Equation 4.6 to obtain the equation

for nondimensional active cofilin in the edge compartment

$$\frac{dc_a^E}{dt} = \frac{\omega D}{V^E}[c_a^I - c_a^E] + d_{C2}c_2^E + k_{off}c_f^E - (k_{on}F)c_a^E - k_p c_a^E + k_{dp}c_p^E + k_{ma}c_m^E \\ -k_{am}c_a^E - k_{Ap2}p_2 c_a^E + d_{hyd}(plc-1)c_2^E. \quad (4.9)$$

Note that the compartment volume consideration affects the scaled equation only by a concentration, or "dilution" effect in the exchange term.

3. **Dynamics of active cofilin in the interior:** The cofilin released into the edge compartment can be contained there by to membrane or filament associated dynamics, but can also transition into the interior compartment of the cell. We consider the large interior compartment of the cell to be well-mixed, as characterized by fast diffusion rates in the cytosol of the cell.

In the interior compartment, we assume cofilin cycles between different forms based on equilibrium interactions between active, monomer-bound, and phospho-cofilin. We assume transition rate constants to be equivalent to transition rates proposed at the edge of the cell. Since the relative volumes of the interior to the edge compartments can differ by up to two orders of magnitude, molecules that transition into the interior compartment are diffused due to the increase in relative volume. Thus, concentrations of interior pools will be relatively constant in the absence of a large release of cofilin molecules from on of the edge pools (ie. such as the release of C_2 following EGF stimulation).

The equation for active cofilin in the interior compartment is

$$\frac{d(V^I C_A^I)}{dt} = \underbrace{-\omega D\left[C_A^I - C_A^E\right]}_{source/loss\ due\ to\ diffusion} \underbrace{- k_p V^I C_A^I + k_{dp} V^I C_P^I}_{phos-dephosphorylation} + \underbrace{k_{ma} V^I C_M^I - k_{am} V^I C_A^I}_{off-on-monomer}, \quad (4.10)$$

where transition rates are as described previously. We scale Equation 4.10, as in Equation 4.6, to obtain the equation for nondimensional local concentration of active interior cofilin

$$\frac{dc_a^I}{dt} = -\frac{\omega D}{V^I}[c_a^I - c_a^E] - k_p c_a^I + k_{dp}c_p^I + k_{ma}c_m^I - k_{am}c_a^I. \quad (4.11)$$

4. **Dynamics of Barbed Ends:**

We use the full (non-approximated) barbed end equation from Section 2.5 of Chapter 2 to a generate a more complete picture of barbed end dynamics. We work with the non-approximated barbed end steady state equation

$$B_{rest} = \frac{P_B + \alpha k_{sev} C_{F,rest}}{k_{cap}},$$

and normalize Equation 3.17 , similar to the method of Section 2.5, such that $B(t) = B_{rest} \cdot b(t)$

$$\frac{db}{dt} = A k_{sev}[\left(\frac{c_f}{\phi_F}\right)^n - 1] - k_{cap}[b - 1] \tag{4.12}$$

where parameters A, k_{sev}, and k_{cap} are as described previously, and ϕ_F is the scaled resting steady state of filament-bound cofilin, $\phi_F = c_{f,rest}$.

The analysis of model parameters in described briefly in Section 4.5, alternatively readers can skip to the outline of parameters used in Tables 4.2 and 4.3.

4.4 Compartmental Model Summary

With these simplifications, we can rewrite the model equations in their reduced and normalized form

$$\begin{aligned}
\frac{dplc}{dt} &= d_{PLC}(\tilde{I}_{stimPLC}(t) + 1 - plc), && (4.13)\\
\frac{dp_2}{dt} &= d_{P2}(1 - p_2 - \tilde{d}_{hyd}(plc-1)p_2), && (4.14)\\
\frac{dc_2^E}{dt} &= k_{Pp2}p_2c_p^E + k_{Ap2}p_2c_a^E - d_{C2}c_2 - d_{hyd}(plc-1)c_2, && (4.15)\\
\frac{dc_a^E}{dt} &= \frac{\omega D}{V^E}[c_a^I - c_a^E] + d_{C2}c_2 + k_{off}c_f - (k_{on}F)c_a^E - k_pc_a^E + k_{dp}c_p^E + k_{ma}c_m^E \\
&\qquad -k_{am}c_a^E - k_{Ap2}p_2c_a^E + d_{hyd}(plc-1)c_2, && (4.16)\\
\frac{dc_f^E}{dt} &= (k_{on}F)c_a - k_{off}c_f - k_{sev}\phi_F\left(\frac{c_f}{\phi_F}\right)^n, && (4.17)\\
\frac{dc_m^E}{dt} &= \frac{\omega D}{V^E}[c_m^I - c_m^E] + k_{sev}\phi_F\left(\frac{c_f}{\phi_F}\right)^n - k_{mp}c_m^E + k_{pm}c_p^E - k_{ma}c_m^E, + k_{am}c_a^E && (4.18)\\
\frac{dc_p^E}{dt} &= \frac{\omega D}{V^E}[c_p^I - c_p^E] + k_pc_a^E - k_{dp}c_p^E + k_{mp}c_m^E - k_{pm}c_p^E - k_{Pp2}p_2c_p^E, && (4.19)\\
\frac{dc_a^I}{dt} &= -\frac{\omega D}{V^I}[c_p^I - c_p^E] - k_pc_a^I + k_{dp}c_p^I + k_{ma}c_m^I - k_{am}^Ic_a^I, && (4.20)\\
\frac{dc_m^I}{dt} &= -\frac{\omega D}{V^I}[c_m^I - c_m^E] - k_{mp}c_m^I + k_{pm}c_p^I - k_{ma}c_m^I + k_{am}c_a^I, && (4.21)\\
\frac{dc_p^I}{dt} &= -\frac{\omega D}{V^I}[c_p^I - c_p^E] + k_pc_a^I - k_{dp}c_p^I + k_{mp}c_m^I - k_{pm}c_p^I, && (4.22)\\
\frac{db}{dt} &= k_{cap}(1-b) + Ak_{sev}\phi_F\left(\frac{c_f}{\phi_F}\right)^n. && (4.23)
\end{aligned}$$

Notice that the reduced cofilin equations form a closed system when multiplied by the respective volume fractions of each compartment, such that

$$v^E \cdot \left[\frac{dc_2}{dt} + \frac{dc_a^E}{dt} + \frac{dc_f}{dt} + \frac{dc_m^E}{dt} + \frac{dc_p^E}{dt}\right] + v^I \cdot \left[\frac{dc_a^I}{dt} + \frac{dc_m^I}{dt} + \frac{dc_p^I}{dt}\right] = 0.$$

4.5 Model Parameter Analysis

As outlined in Section 3.4.2, we have information referring to the concentrations of various cofilin pools at rest.

We first make some assumptions necessary for model identification.

- We first consider the assumption that the freely diffusing cofilin forms are at equal concentrations in the edge and interior compartments at rest. This allows us to reduce the compartment exchange term from the steady state equations.[1]

- We assume that transition rates between cofilin forms are equivalent in the respective compartments. Effectively, we assume that the cellular complexes required for each transition are equally abundant and active in the edge and the interior of the cell. This assumption may be accurate for some cofilin processes (such as LIM kinase-mediated phosphorylation) and very inaccurate for others (ie. monomer-binding). The transition rates will be considered independently in a later model reduction.

4.5.1 Steady State Analysis

The steady state equations provide constraints on parameters. We set derivatives of Equations 4.15-4.22 to zero and examine rest state conditions. From Equation 4.15

$$c^E_{2,rest} = \frac{1}{d_{C2}} \cdot [k_{Pp2} c^E_{p,rest} + k_{Ap2} c^E_{a,rest}]. \tag{4.24}$$

Under the assumption $c^E_{a,rest} << 1$ as described in Chapter 3, this gives the approximate relationship

$$\frac{k_{p2}}{d_{C2}} \approx \frac{c^E_{2,rest}}{c^E_{p,rest}},$$

indicating that the binding rate of phospho-cofilin to PIP_2 at the membrane must be significantly higher than the C_2 decay rate in order to maintain the large local concentration of PIP_2-bound cofilin.

We assume here that free diffusing forms of cofilin have the same concentration in the edge and interior compartments. The steady state equations of these forms account only for the source and loss terms of the pool, so from Equation 4.16, the resting level of active cofilin in the edge compartment is

$$c^E_{a,rest} = \frac{d_{C2} c_{2,rest} + k_{off} c_{f,rest} + k_{ma} c^E_{m,rest} + k_{dp} c^E_{p,rest}}{k_{Ap2} + k_{on} F + k_{am} + k_p}. \tag{4.25}$$

[1] The no net flux simplification will have to be reviewed in later models. It is possible that rest conditions could lead to opposed standing gradients at the cell edge such that the net flux between compartments is zero.

The steady state equation for filament-bound cofilin, from Equation 4.17, is much simpler, since our model includes just one known source

$$c^E_{f,rest} = \frac{k_{on}F}{k_{off} + k_{sev}} \cdot c^E_{a,rest}, \tag{4.26}$$

which can be rearranged to obtain the relationship

$$\frac{c^E_{f,rest}}{c^E_{a,rest}} = \frac{k_{on}F}{k_{off} + k_{sev}}.$$

This implies that binding parameters must exceed the loss rates by some magnitude to maintain the relatively high local concentration of filament-bound cofilin, ($c^E_{f,rest} >> c^E_{a,rest}$) in the edge compartment at rest.

Based on Equation 4.18, we find

$$c^E_{m,rest} = \frac{k_{sev}c^E_{f,rest} + k_{am}c^E_{a,rest} + k_{pm}c^E_{m,rest}}{k_{mp} + k_{ma}}, \tag{4.27}$$

where the severing term is expected to be low at rest.

Equation 4.19 implies the concentration of phosphorylated cofilin in the edge compartment at rest satisfies

$$c^E_{p,rest} = \frac{k_p c^E_{a,rest} + k_{mp}c^E_{m,rest}}{k_{dp} + k_{pm} + k_{p2}}. \tag{4.28}$$

The equations of cofilin forms in the interior compartment each have two source terms and two loss terms. Based on Equation 4.20, the relative concentration of active cofilin in the interior is given by

$$c^I_{a,rest} = \frac{k_{dp}c^I_{p,rest} + k_{ma}c^I_{m,rest}}{k_p + k_{am}}. \tag{4.29}$$

Similarly, from Equation 4.21, the interior monomer-bound cofilin at rest satisfies

$$c^I_{m,rest} = \frac{k_{pm}c^I_{p,rest} + k_{am}c^I_{a,rest}}{k_{mp} + k_{ma}}. \tag{4.30}$$

And finally, the concentration of phospho-cofilin in the interior, from Equation 4.22, must satisfy

$$c^I_{p,rest} = \frac{k_p c^I_{a,rest} + k_{mp} c^I_{m,rest}}{k_{dp} + k_{pm}}. \tag{4.31}$$

4.5.2 Model Parameter Estimation

Under the assumption of equal concentrations in the edge and interior compartments, we can combine equations for respective forms of cofilin and reduce parameters. Equating the edge and interior concentrations of monomer-bound cofilin at rest, Equations 4.27 and 4.30, and reducing the equivalent loss terms obtains the relationship

$$k_{sev} c^E_{f,rest} + k_{am} c^E_{a,rest} + k_{pm} c^E_{p,rest} = k_{pm} c^I_{p,rest} + k_{am} c^I_{a,rest}, \tag{4.32}$$

which reduces to

$$k_{sev} c^E_{f,rest} = 0.$$

Since $c^E_{f,rest} > 0$, this implies $k_{sev} = 0$. This zero severing rate contradiction could be a result of any one of our model assumptions. Equation 4.32 suggests that one or more of the simplifications should be reconsidered in future models. Some suggested modifications are:

1. Variation in parameters between the edge and interior compartments. This revision to our initial assumptions is supported by the dependence of cellular complexes on the rate of cofilin transition between forms. The concentrations of such complexes may vary in the edge and interior of the cell.

2. The assumption of equal concentrations of cofilin forms between the edge and interior should be reviewed. This may be most easily approached in a one-dimensional spatial framework as here we work with local average cofilin concentrations in each compartment.

Here I address the contradiction from Equation 4.32 by considering the first modification, and revise the parameter consistency assumption in the following section.

4.5.3 Distinct Transition Rates in Compartments

In Equation 4.32, both the monomer-binding rate k_{am}, and the combined dephosphorylation-monomer-binding rate k_{pm} are assumed to be equivalent in the edge and interior of the cell. However, both of these processes are dependent on the concentration of G-actin available for binding. It has been shown in both experimental and analytical work that concentrations of G-actin are higher in the cell interior due to higher filaments breakdown, and are depleted at the cell edge where there is an increased polymerization rate [26**?**].

We assume that the cofilin-G-actin association rate is negligible in the edge compartment, such that

$$k_{am}^{E} \approx 0, \quad k_{pm}^{E} \approx 0. \tag{4.33}$$

We rewrite Equation 4.32 with the notation k_{am}^{I} and k_{pm}^{I}, to differentiate between these rates. Therefore,

$$k_{sev}c_{f,rest}^{E} + k_{am}^{E}c_{a,rest}^{E} + k_{pm}^{E}c_{m,rest}^{E} = k_{pm}^{I}c_{p,rest}^{I} + k_{am}^{I}c_{a,rest}^{I}.$$

This approximation obtains the relationship

$$k_{sev}c_{f,rest}^{E} \approx k_{pm}^{I}c_{p,rest}^{I} + k_{am}^{I}c_{a,rest}^{I}. \tag{4.34}$$

The positivity of rate constants and the condition imposed by Equation 4.34 set restrictions on parameter magnitudes. As outlined in previous chapters, we expect filament severing by cofilin to be low in the cell at rest. Here, the magnitude of k_{sev} must be significant enough to maintain $k_{pm}^{I} > 0$ and $k_{am}^{I} > 0$.

Outlined in previous chapters, we assume a very low concentration of active cofilin in the resting cell. In Chapter 3, we used the value $c_{a,rest} = 0.01$ and determined the resulting severing parameter, k_{sev}, by applying model constraints (Equation 3.34). Here we resolve the constraint of Equation 4.34 by applying a lower rest state concentration of active cofilin $c_{a,rest} \approx 10^{-4}$. This is motivated and supported by personal communication with J. Condeelis where he predicts

a near-zero rest concentration of active cofilin.

In a similar manner, the remaining rest state relationships, Equations 4.28 and 4.31 to obtain the phosphorylation and dephosphorylation parameter relationships. The remaining parameters are constrained by Equations 4.25 and 4.29. The parameter estimates outlined in Table 4.3 were calculated using the temporal data described in Section 3.4.2, the volume assumptions outlined in the Appendix, and the scaled resting concentrations, and parameter relationships described here.

4.6 Further Proposed Simplifying Assumptions

The number of parameters introduced by this expansion creates a model identification problem in the absence of additional experimental data. To proceed with parameter estimation and model simulations, we must make some critical assumptions to simplify equations and reduce the number of unknown parameters to be analyzed. Here we start by identifying a large number (upper bound) of simplifications. These should be reviewed in future works.

We summarize the parameter simplifications, motivated by assumptions described in Section 4.5.3, and by conversations with J. Condeelis.

1. Following Section 4.5.3, we assume that monomer binding of both active and phospho-cofilin occurs at a very low rate in the edge compartment. We differentiate between edge and interior parameters, as in Equation 4.33, such that

$$k_{am}^{E} \approx 0, \quad k_{pm}^{E} \approx 0.$$

   Interior rates are denoted as

$$k_{am}^{I}, \quad k_{pm}^{I}.$$

2. From conversations with J. Condeelis, we identify that phosphorylation rates of active and monomer-bound cofilin are indistinguishable in the cell. Effectively, this is an assumption that the monomer-stripping step is negligible within the phosphorylation process, possible

due to a combined LIM kinase-SSH complex. The phosphorylation rates are expressed as

$$k_{mp} \approx k_p.$$

3. We also identify that rebinding of active cofilin to PIP_2 at the membrane occurs at a very low rate, due to the instability of active cofilin, and its tendency to diffuse away from membrane contact after its release. We assume

$$k_{Ap2} \approx 0,$$

eliminating this interaction from the model.

We apply these simplifying assumptions to the compartmental model. The revised schematic of cofilin interconversion between forms is shown in Figure 4.2. Parameter values obtained from calculations in this section, including these simplifying assumptions are outlined in Table 4.3.

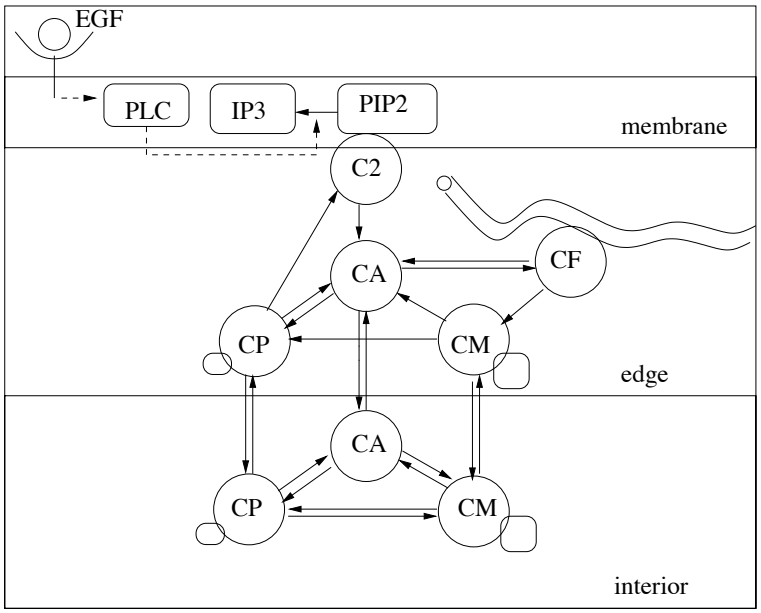

Figure 4.2: Schematic of proposed reduced temporal model of cofilin pathway with reduced assumptions outlined in Section 4.6.

4.7 Reduced Model Summary

Here we summarize model variables and their resting state levels in Table 4.2, and parameter values used to simulate the model equations in Table 4.3.

Cofilin Pool	Description	Resting Level	Source
C_2^E	PIP_2-bound cofilin	$2.00 \cdot C_{tot}$	discussion
C_A^E	active cofilin in edge	$10^{-4} \cdot C_{tot}$	approximated in model
C_F^E	F-actin-bound cofilin	$0.40 \cdot C_{tot}$	van Rheenen 2007
C_M^E	G-actin-bound cofilin in edge	$0.68 \cdot C_{tot}$	conservation assumption
C_P^E	phosphorylated cofilin in edge	$0.20 \cdot C_{tot}$	Song 2006
C_A^I	active cofilin in interior	$10^{-4} \cdot C_{tot}$	approximated in model
C_M^I	G-actin-bound cofilin in interior	$0.68 \cdot C_{tot}$	conservation assumption
C_P^I	phosphorylated cofilin in interior	$0.20 \cdot C_{tot}$	Song 2006
C_{tot}	average cofilin concentration	$10\mu M$	Pollard 2000
V^E	volume of edge compartment	$50\mu\text{m}^3$	Mogilner Keshet 2002
V^I	volume of interior compartment	$950\mu\text{m}^3$	Mogilner Keshet 2002

Table 4.2: Cofilin forms in the edge and interior compartments, as in Table 4.1, repeated here for the purpose of summarizing conclusions. We designate volume of the edge and interior compartments (shown in the Appendix) and summarize rest concentrations defined relative to average cellular cofilin concentration. Note that the local concentration, C_2^E is higher than the average cellular cofilin concentration due to the large number of cofilin molecules crowded in the small edge compartment.

Parameter	Description	Value	Source
$\tilde{I}_{stim}$	PLC activation rate	1.5	Mouneimne 2004
d_{PLC}	PLC decay rate	$0.018s^{-1}$	Mouneimne 2004
d_{P2}	PIP_2 resting hydrolysis	$0.002s^{-1}$	van Rheenen 2007
d_{hyd}	PLC-PIP_2 hydrolysis rate	$0.01s^{-1}$	van Rheenen 2007
V_{tot}	total cell volume	$1000\mu\text{m}^3$	estimated in Appendix
V^E	edge compartment volume	$50\mu\text{m}^3$	estimated in Appendix
k_{Pp2}	PIP_2-binding of phospho-cofilin	$0.020s^{-1}$	estimated by model
k_{Ap2}	PIP_2-binding of active cofilin	0	assumption
d_{C2}	PIP_2-cofilin decay rate	$0.002s^{-1}$	assumption
k_{off}	cofilin-F-actin off-rate	$0.016s^{-1}$	van Rheenen 2007 required by model
$k_{on}F$	Filament binding rate	$106.6s^{-1}$	estimated by model
k_{sev}	Cofilin severing rate	$0.0112s^{-1}$	required by model
k_{ma}	monomer-cofilin off-rate	$0.0083s^{-1}$	estimated in model
k_{am}^I	monomer-cofilin binding in interior	$4.79s^{-1}$	estimated in model
k_{am}^E	monomer-cofilin binding in edge	0	assumption
k_p	phosphorylation of active cofilin	$0.0118s^{-1}$	estimated by model
k_{mp}	phosphorylation of monomer-cofilin	$0.0118s^{-1}$	assumption
k_{dp}	cofilin dephosphorylation	$0.020s^{-1}$	estimated by model
k_{cap}	barbed end capping rate	$1s^{-1}$	Dawes 2006
α	unit conversion factor	$600\mu M^{-1}\mu m^{-3}$	Mogilner, LEK 2002
A	scaling factor	1000	Lorenz 2004

Table 4.3: Parameter estimates for revised compartmental cofilin pathway model

4.8 Simulations of Revised Compartmental Model

We show some preliminary results here based on our current parameter estimates. We initialize the system at the resting steady states outlined in Table 4.2, and stimulate using parameter values in Table 4.3 via addition of an EGF signal at 60s, removed at 120s.

We obtain the same PLC and PIP_2 results, shown in Figure 3.5 and simulate the effect of these dynamics on the cofilin pools in the edge and interior compartments, shown in the top and bottom panels of Figure 4.8.1 respectively. Figure 4.4 shows these same cofilin results, but displays profiles as fractions of total molecules of cofilin, for example $v^E \cdot c_i^E = V^E \cdot C_i^E / V_{tot} \cdot C_{tot}$. Two cases of barbed end simulation results are shown in Figure 4.5 for parameters in Table 4.3. The top panel uses low hydrolization rate $d_{hyd} = 0.01s^{-1}$, as estimated by experimental results. The bottom panel displays results for the increased hydrolysis, $d_{hyd} = 0.04s^{-1}$, as per discussions with J. Condeelis.

4.8.1 Discussion of Compartmental Model

The compartmental model expands the well-mixed model in several respects. The compartmental framework provides a more accurate representation of the cell, accounting for the high local concentrations of PIP_2-bound and filament-bound cofilin. The added complexity of interactions and cellular geometry considerations introduce challenges in parameter constraints. Furthermore, the lack of available experimental data requires assumptions to simplify the model and identify parameters.

However, in view of these increased complexities, and the distinct differences in the dynamics of cofilin pools, the barbed end results of the compartmental and well-mixed models, Figures 3.8, and 4.5 are remarkably similar. This may indicate that the interactions introduced in the compartmental are not essentia to generate the barbed end amplification. The simplified cofilin interactions of the well-mixed system should be investigated under the compartmental framework to confirm this hypothesis. The compartmental model also exhibits similar limitations as those described in Chapter 3. The increase of filament-bound cofilin increases only to a maximum of 1.4 relative to rest levels, failing to reach the 2-fold increase shown in Figure 1.3 from

van Rheenen (2007). We propose several experimental considerations to investigate these issues in the discussion of Section 5.2.1 of Chapter 5.

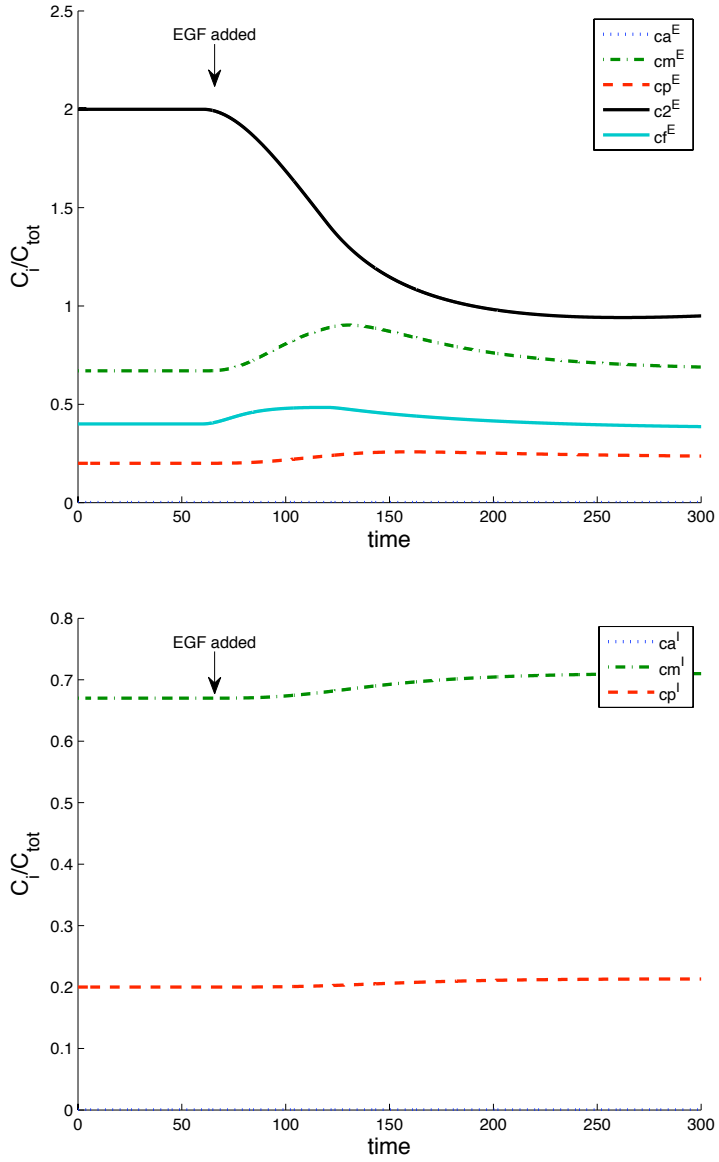

Figure 4.3: Simulations of cofilin concentrations, Equations 4.15-4.22, in the edge and interior compartment relative to average cofilin concentration C_{tot} for parameter settings found in Table 4.3 and discussed in the text. Cofilin pools are initiated at resting concentrations, a stimulus (EGF) is added at 60s and removed at 120s. Top: Dynamics of cofilin pools in the edge compartment. Bottom: Dynamics of cofilin pools in interior. Notice small and shallow increase in filament bound cofilin at the edge. This is due to a high rest severing rate, and relatively high phosphorylation of active cofilin. The resulting barbed end peak (Figure 4.5) is significantly less than the 12 fold increase (even with $n = 7$) and does not exhibit the sharp increase and decrease observed in experiments (Mouneimne 2004) [24].

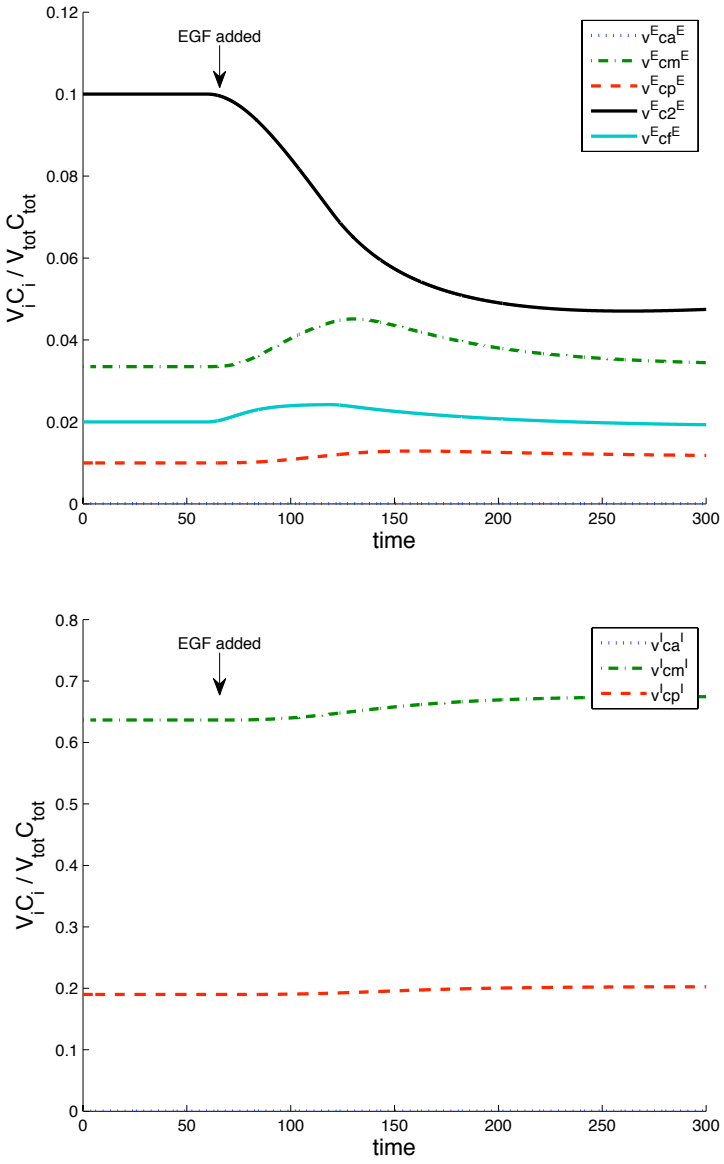

Figure 4.4: Time profiles of amount of cofilin as fractions of total cellular cofilin (# of molecules) for parameters from Table 4.3. Top: Edge compartment dyamics, Bottom: Interior compartment dynamics. Simulations are the same as in Figure 4.8.1, but concentrations are scaled by relative volumes of compartments.

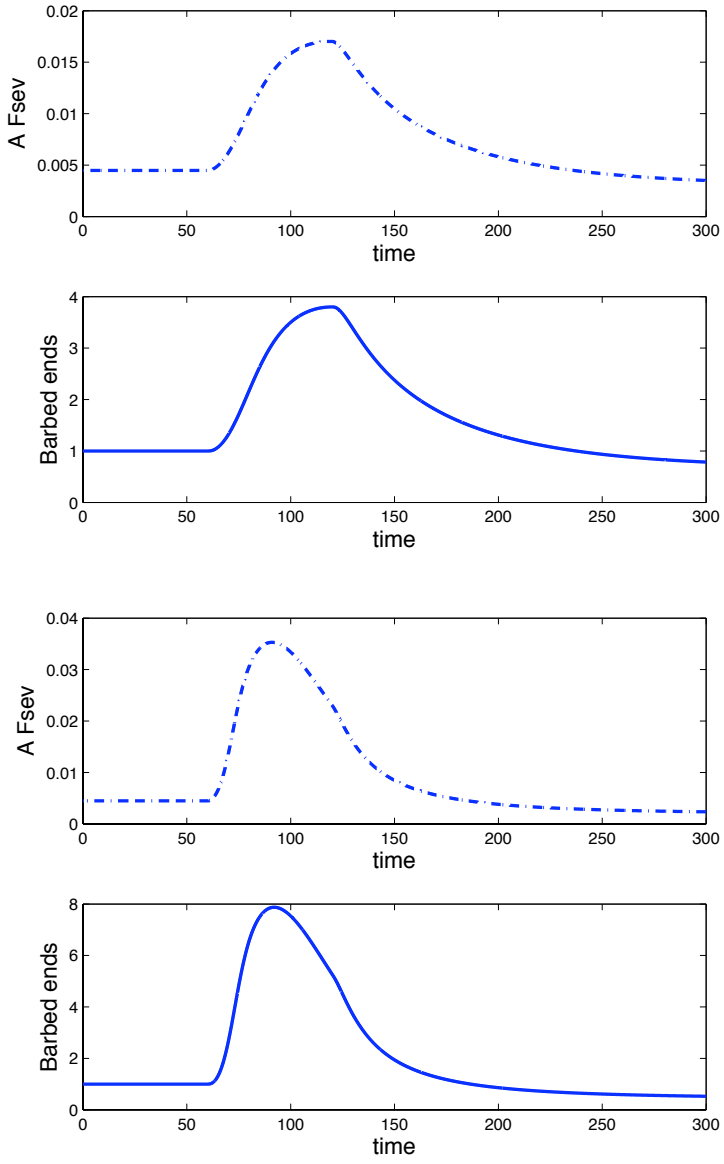

Figure 4.5: Results of the compartmental model for parameters in Table 4.3, demonstrating two cases of PIP_2 hydrolysis, 60% decrease (Top), and 95% decrease (Bottom). Top: Rate of filament-severing by cofilin (top curve), and resulting barbed end profiles (bottom curve) for $d_{hyd} = 0.01s^{-1}$, shown as relative density over resting barbed end concentration. Notice the shallow barbed end amplification of approximately 3-fold increase within 60s of addition of EGF stimulus with slow decay back to resting barbed end density. Bottom: Rate of filament-severing by cofilin (top curve), and resulting fold increase in barbed ends (bottom curve) for increased PIP_2 hydrolysation rate $d_{hyd} = 0.04s^{-1}$. Amplification increase to approximately 8-fold, similar to the result of the well-mixed model of Chapter 3.

Chapter 5

Discussion of Cofilin Model Results

Recent experimental work indicates that cofilin activity determines the sites of actin polymerization and resulting cell movement in metastasizing mammary tumour cells [7, 15]. Previously hypothesized to be important only for filament disassembly, as strictly an actin depolymerizing factor [4, 5], cofilin is now unexpectedly at the cell motility forefront as a key determinant of a cell's ability to detect chemoattractant gradients and direct cell protrusion. Furthermore, cofilin may interact synergistically with the Arp2/3 complex to promote actin nucleation, and thereby influence overall cell polarity.

Though substantial ground has been made experimentally to identify the underlying mechanisms of cofilin activation in the cell [31, 33], there are many open questions and difficult obstacles to overcome in order to gain a more complete understanding of cancer cell metastasis. The modeling work described in this thesis represents one such initial step in the critical analysis of this important activity cycle.

5.1 Discussion of Temporal Model Results

The models discussed in Chapters 2-4 determine important interactions with the cofilin activity cycle and propose the significant model considerations for simulation of the initial cofilin-dependent peak of barbed ends in a stimulated cell. Both the well-mixed and compartmental models of Chapters 3 and 4 respectively can reproduce temporally accurate barbed end peaks observed in recent experiments [15, 19, 23] (reproduced in Figure 1.4). In both cases, the magnitude of the barbed end readout of model simulations is robust to most parameters, including

severing rate parameter assumptions. A barbed end peak of the 10-fold magnitude observed under certain experimental conditions [23], requires almost complete reduction of PIP_2 levels (Figures 3.11, and 4.5).

The similar barbed end results obtained from the well-mixed and compartmental models indicate that some of the complexities introduced in Chapter 4 do not play a significant role in barbed end generation. These should be investigated in future work such that a spatial model can be appropriately simplified to include only the essential level of complexity.

5.2 Proposed Future Considerations

The models described in this thesis facilitate insight about future considerations for both modeling and experimental work.

5.2.1 Issues for Experimental Investigation

The models described in this thesis facilitate insight about future considerations for both modeling and experimental work. A residual challenge stemmed from the discrepancy between model parameter constraints and experimentally proposed relative magnitudes of the rate that cofilin unbinds from (k_{off}) and severs (k_{sev}) an actin filament. An example of such a constraint relationship is outlined in Section 4.5.2. In lieu of conclusive experimental data, modelers must enforce system assumptions to resolve constraints. Experimental work to investigate the relationship between filament-binding, severing and G-actin binding of cofilin in the cell periphery would be invaluable to either support or negate model assumptions.

The shortfall of both models to reproduce the observed 2-fold amplification of filament-bound cofilin at $60s$ following stimulation requires further attention. We suppose that this issue stems from the filament severing rate used in both models, motivated in Section 2.5. Through personal communication with J. Condeelis, and supported by recent work outlined in Frantz (2008), we identify that filament severing *in vivo* is highly dependent on pH levels in the cell [14]. Stimulation with EGF induces a pH change through a pathway independent of the cofilin activity

cycle studied in our model. This effect is proposed to delay the effect of the amplified severing, and could result in a build up of filament-bound cofilin before the rapid filament-severing occurs. Such a hypothesis requires further experimental motivation. For example, a time profile of filament-bound cofilin density would be beneficial to test model validity. Currently the only *in vivo* C_F data describe the density at $0s$ and $60s$ following EGF stimulation (Figure 1.3 from van Rheenen (2007)).

5.2.2 Future Modeling Work

Further research into the cofilin activity cycle is imperative. Due to the complexity and cost of the experimental study of mammary tumour cells *in vivo*, the medical and societal importance of understanding the metastatic phenotype notwithstanding, research in this field demands the collaboration of experimentalists and modelers. As stated, we propose the models outlined in this thesis as a foundational study into the temporal dynamics of the cofilin activity pathway. We focused here on the mechanisms necessary to produce the EGF-induced burst of barbed ends produced by increased cofilin activity. There are many potential directions for future modeling work.

A logical first step would be to extend the model to include spatial properties, by analysing a one dimensional transect of the cell. A model of this form would facilitate a more accurate representation of the dynamic filament density of the cell. Spatial profile data of the barbed end density produced by the cofilin cycle has been developed recently [23, 24]. An important distinction from previous spatial models of cell motility in keratocytes [9, 10], the barbed end peak produced by cofilin is transient, and would not generate steady state traveling wave solutions. This can be traced to the inherently different methods of migration of keratocytes and cancer cells.

Further investigation into the role of the cofilin activity cycle in the overall metastatic phenotype of cancer cells is also critically important. The advancement of the big picture of how cancer cells migrate and invade is critical to the identification of the important targets to inhibit the spread, and consequent fatality of cancer in the body.

5.2.3 Other Perspectives

The cofilin activity cycle has emerged as a critical regulator of membrane protrusion; however, tumour cell migration and invasion has been shown to depend on the activity status of several signalling pathways, including the N-Wasp and MENA pathway, critical for both protrusion and the necessary breakdown of the extracellular matrix [20]. It is through fine coordination of the respective signalling networks that cancer cells are able to produce sufficient protrusive force and enzymatic activity to migrate into blood vessels and invade body tissues. As the understanding of N-Wasp and MENA signalling pathways develop experimentally, theoretical investigation of the relationships within the regulation network will be important to test hypotheses and propose interactions to be analysed experimentally.

Bibliography

[1] Ernesto Andrianantoandro and Thomas D Pollard. Mechanism of actin filament turnover by severing and nucleation at different concentrations of adf/cofilin. *Mol Cell*, 24(1):13–23, Oct 2006.

[2] L Blanchoin and T D Pollard. Mechanism of interaction of acanthamoeba actophorin (adf/cofilin) with actin filaments. *J Biol Chem*, 274(22):15538–46, May 1999.

[3] Wenxiang Cao, Jim P Goodarzi, and Enrique M De La Cruz. Energetics and kinetics of cooperative cofilin-actin filament interactions. *J Mol Biol*, 361(2):257–67, Aug 2006.

[4] M F Carlier, V Laurent, J Santolini, R Melki, D Didry, G X Xia, Y Hong, N H Chua, and D Pantaloni. Actin depolymerizing factor (adf/cofilin) enhances the rate of filament turnover: implication in actin-based motility. *J Cell Biol*, 136(6):1307–22, Mar 1997.

[5] M F Carlier and D Pantaloni. Control of actin dynamics in cell motility. *J Mol Biol*, 269(4):459–67, Jun 1997.

[6] A E Carlsson. Stimulation of actin polymerization by filament severing. *Biophys J*, 90(2):413–22, Jan 2006.

[7] A Y Chan, M Bailly, N Zebda, J E Segall, and J S Condeelis. Role of cofilin in epidermal growth factor-stimulated actin polymerization and lamellipod protrusion. *J Cell Biol*, 148(3):531–42, Feb 2000.

[8] Lingfeng Chen, Chris Janetopoulos, Yi Elaine Huang, Miho Iijima, Jane Borleis, and Peter N Devreotes. Two phases of actin polymerization display different dependencies on pi(3,4,5)p3 accumulation and have unique roles during chemotaxis. *Mol Biol Cell*, 14(12):5028–37, Dec 2003.

[9] Adriana T Dawes, G Bard Ermentrout, Eric N Cytrynbaum, and Leah Edelstein-Keshet. Actin filament branching and protrusion velocity in a simple 1d model of a motile cell. *J Theor Biol*, 242(2):265–79, Sep 2006.

[10] Adriana T Dawes and Leah Edelstein-Keshet. Phosphoinositides and rho proteins spatially regulate actin polymerization to initiate and maintain directed movement in a one-dimensional model of a motile cell. *Biophys J*, 92(3):744–68, Feb 2007.

[11] Enrique M De La Cruz. Cofilin binding to muscle and non-muscle actin filaments: isoform-dependent cooperative interactions. *J Mol Biol*, 346(2):557–64, Feb 2005.

[12] Vera DesMarais, Ilia Ichetovkin, John Condeelis, and Sarah E Hitchcock-DeGregori. Spatial regulation of actin dynamics: a tropomyosin-free, actin-rich compartment at the leading edge. *J Cell Sci*, 115(Pt 23):4649–60, Dec 2002.

[13] Vera DesMarais, Frank Macaluso, John Condeelis, and Maryse Bailly. Synergistic interaction between the arp2/3 complex and cofilin drives stimulated lamellipod extension. *J Cell Sci*, 117(Pt 16):3499–510, Jul 2004.

[14] Christian Frantz, Gabriela Barreiro, Laura Dominguez, Xiaoming Chen, Robert Eddy, John Condeelis, Mark J S Kelly, Matthew P Jacobson, and Diane L Barber. Cofilin is a ph sensor for actin free barbed end formation: role of phosphoinositide binding. *J Cell Biol*, 183(5):865–79, Dec 2008.

[15] Mousumi Ghosh, Xiaoyan Song, Ghassan Mouneimne, Mazen Sidani, David S Lawrence, and John S Condeelis. Cofilin promotes actin polymerization and defines the direction of cell motility. *Science*, 304(5671):743–6, Apr 2004.

[16] Vitaliy Y Gorbatyuk, Neil J Nosworthy, Scott A Robson, Naresh P S Bains, Mark W Maciejewski, Cris G Dos Remedios, and Glenn F King. Mapping the phosphoinositide-binding site on chick cofilin explains how pip2 regulates the cofilin-actin interaction. *Mol Cell*, 24(4):511–22, Nov 2006.

[17] Ravine A Gungabissoon and James R Bamburg. Regulation of growth cone actin dynamics by adf/cofilin. *J Histochem Cytochem*, 51(4):411–20, Apr 2003.

[18] Philip A Kuhlman. Dynamic changes in the length distribution of actin filaments during polymerization can be modulated by barbed end capping proteins. *Cell Motil Cytoskeleton*, 61(1):1–8, May 2005.

[19] Mike Lorenz, Vera DesMarais, Frank Macaluso, Robert H Singer, and John Condeelis. Measurement of barbed ends, actin polymerization, and motility in live carcinoma cells after growth factor stimulation. *Cell Motil Cytoskeleton*, 57(4):207–17, Apr 2004.

[20] Mike Lorenz, Hideki Yamaguchi, Yarong Wang, Robert H Singer, and John Condeelis. Imaging sites of n-wasp activity in lamellipodia and invadopodia of carcinoma cells. *Curr Biol*, 14(8):697–703, Apr 2004.

[21] Alex Mogilner and Leah Edelstein-Keshet. Regulation of actin dynamics in rapidly moving cells: a quantitative analysis. *Biophys J*, 83(3):1237–58, Sep 2002.

[22] K Moriyama, K Iida, and I Yahara. Phosphorylation of ser-3 of cofilin regulates its essential function on actin. *Genes Cells*, 1(1):73–86, Jan 1996.

[23] Ghassan Mouneimne, Vera DesMarais, Mazen Sidani, Eliana Scemes, Weigang Wang, Xiaoyan Song, Robert Eddy, and John Condeelis. Spatial and temporal control of cofilin activity is required for directional sensing during chemotaxis. *Curr Biol*, 16(22):2193–205, Nov 2006.

[24] Ghassan Mouneimne, Lilian Soon, Vera DesMarais, Mazen Sidani, Xiaoyan Song, Shu-Chin Yip, Mousumi Ghosh, Robert Eddy, Jonathan M Backer, and John Condeelis. Phospholipase c and cofilin are required for carcinoma cell directionality in response to egf stimulation. *J Cell Biol*, 166(5):697–708, Aug 2004.

[25] Michiru Nishita, Chinatsu Tomizawa, Masahiro Yamamoto, Yuji Horita, Kazumasa Ohashi, and Kensaku Mizuno. Spatial and temporal regulation of cofilin activity by lim kinase and slingshot is critical for directional cell migration. *J Cell Biol*, 171(2):349–59, Oct 2005.

[26] T D Pollard, L Blanchoin, and R D Mullins. Molecular mechanisms controlling actin filament dynamics in nonmuscle cells. *Annu Rev Biophys Biomol Struct*, 29:545–76, 2000.

[27] Ewa Prochniewicz, Neal Janson, David D Thomas, and Enrique M De la Cruz. Cofilin increases the torsional flexibility and dynamics of actin filaments. *J Mol Biol*, 353(5):990–1000, Nov 2005.

[28] F Ressad, D Didry, G X Xia, Y Hong, N H Chua, D Pantaloni, and M F Carlier. Kinetic analysis of the interaction of actin-depolymerizing factor (adf)/cofilin with g- and f-actins. comparison of plant and human adfs and effect of phosphorylation. *J Biol Chem*, 273(33):20894–902, Aug 1998.

[29] Mazen Sidani, Deborah Wessels, Ghassan Mouneimne, Mousumi Ghosh, Sumanta Goswami, Corina Sarmiento, Weigang Wang, Spencer Kuhl, Mirvat El-Sibai, Jonathan M Backer, Robert Eddy, David Soll, and John Condeelis. Cofilin determines the migration behavior and turning frequency of metastatic cancer cells. *J Cell Biol*, 179(4):777–91, Nov 2007.

[30] P Silacci, L Mazzolai, C Gauci, N Stergiopulos, H L Yin, and D Hayoz. Gelsolin superfamily proteins: key regulators of cellular functions. *Cell Mol Life Sci*, 61(19-20):2614–23, Oct 2004.

[31] Xiaoyan Song, Xiaoming Chen, Hideki Yamaguchi, Ghassan Mouneimne, John S Condeelis, and Robert J Eddy. Initiation of cofilin activity in response to egf is uncoupled from cofilin phosphorylation and dephosphorylation in carcinoma cells. *J Cell Sci*, 119(Pt 14):2871–81, Jul 2006.

[32] Jacco van Rheenen, John Condeelis, and Michael Glogauer. A common cofilin activity cycle in invasive tumor cells and inflammatory cells. *J Cell Sci*, 122(Pt 3):305–11, Feb 2009.

[33] Jacco van Rheenen, Xiaoyan Song, Wies van Roosmalen, Michael Cammer, Xiaoming Chen, Vera Desmarais, Shu-Chin Yip, Jonathan M Backer, Robert J Eddy, and John S Condeelis. Egf-induced pip2 hydrolysis releases and activates cofilin locally in carcinoma cells. *J Cell Biol*, 179(6):1247–59, Dec 2007.

[34] Weigang Wang, Ghassan Mouneimne, Mazen Sidani, Jeffrey Wyckoff, Xiaoming Chen, Anastasia Makris, Sumanta Goswami, Anne R Bresnick, and John S Condeelis. The activity status of cofilin is directly related to invasion, intravasation, and metastasis of mammary tumors. *J Cell Biol*, 173(3):395–404, May 2006.

Appendix

Full Model Equations from Chapter 3

The full model equations in unscaled form are

$$\begin{aligned}
\frac{dPLC}{dt} &= I_{PLC} + I_{stimPLC}(t) - d_{PLC}PLC, && (5.1)\\
\frac{dP_2}{dt} &= I_{P_2} - d_{P2}P_2 - \left(\frac{d_{hyd}}{PLC_{rest}}\right)(PLC - PLC_{rest})P_2, && (5.2)\\
\frac{dC_2}{dt} &= \left(\frac{k_{dp}}{P_{2,rest}}\right)P_2C_P - d_{C2}C_2 - \left(\frac{d_{hyd}}{PLC_{rest}}\right)(PLC - PLC_{rest})C_2, && (5.3)\\
\frac{dC_A}{dt} &= d_{C2}C_2 + k_{off}C_F - (k_{on}F)C_A - k_pC_A + \left(\frac{d_{hyd}}{PLC_{rest}}\right)(PLC - PLC_{rest})C_2, && (5.4)\\
\frac{dC_F}{dt} &= (k_{on}F)C_A - k_{off}C_F - k_{sev}C_{F,rest}\left(\frac{C_F}{C_{F,rest}}\right)^n, && (5.5)\\
\frac{dC_M}{dt} &= k_{sev}C_{F,rest}\left(\frac{C_F}{C_{F,rest}},\right)^n - k_pC_M, && (5.6)\\
\frac{dC_P}{dt} &= k_pC_A + k_pC_M - \left(\frac{k_{dp}}{P_{2,rest}}\right)P_2C_P, && (5.7)\\
\frac{dB}{dt} &= P_B - k_{cap}B + \alpha k_{sev}C_{F,rest}\left(\frac{C_F}{C_{F,rest}}\right)^n. && (5.8)
\end{aligned}$$

with

$$I_{stimPLC}(t) = \begin{cases} I_{stim}\cdot EGF & \text{when stimulated by EGF} \\ 0 & \text{otherwise} \end{cases}$$

and

$$F_{sev}(C_F) = k_{sev}C_{F,rest}\left(\frac{C_F}{C_{F,rest}}\right)^n.$$

By adding together the equations for the cofilin forms, we find that

$$\frac{dC_2}{dt} + \frac{dC_A}{dt} + \frac{dC_F}{dt} + \frac{dC_M}{dt} + \frac{dC_P}{dt} = 0$$

which is a check for conservation of the total cofilin, i.e. for the fact that

$$C_2 + C_A + C_F + C_M + C_P = C_{tot} = \text{constant}.$$

Calculation of Conversion Factor α

Here we describe calculations to obtain the model conversion parameter α. This parameter serves two purposes: to convert between common units of cofilin concentration measurement (μM) and barbed end density (number per μm^2), and to scale the number of cofilin molecules used in a severing event into the number of barbed ends produced.

We first proceed as described in Mogilner and Edelstein-Keshet 2002, [21], to estimate conversion between units of cellular concentration, μM, and common units of barbed end quantification, $\#\mu m^{-2}$. We have

$$1\mu M \approx 10^{-6} \cdot \frac{6\text{x}10^{23}\text{molec}}{L} = \frac{6\text{x}10^{17}\text{molec}}{dm^3} \cdot \frac{10^{-15} dm^3}{1\mu m^3},$$

and therefore,

$$1\mu M \approx 600 \quad \text{moleculesper}\mu\text{m}^3.$$

This relationship gives us a working estimate for conversion between unit volumes,

$$\nu = 600\mu M^{-1}\mu\text{m}^{-3}.$$

Experimental approximations of barbed end density in a resting cell, such as those given in Lorenz (2004) [19] are generally given in units of number per μm^2. This means that we must multiply the parameter ν by the approximate width of the lamellipod. If we approximate the lamellipod width as $\omega \approx 0.200\mu\text{m}$, we obtain a unit conversion parameter

$$\tilde{\nu} = \omega \cdot \nu \approx 120\mu M^{-1}\mu\text{m}^{-2}.$$

It is proposed experimentally that a finite number n, where $n \approx$ 5-7, of bound cofilin molecules are required to force a filament break. We use this assumption throughout Chapters

2-4, and use $n = 7$ in most simulations. Therefore, we approximate the conversion parameter as

$$\alpha = \frac{\tilde{\nu}}{n} \approx 17.1 \mu M^{-1} \mu \text{m}^{-2}.$$

Cell Geometry Calculations from Chapter 4

We now give rough calculations for the volumes of the edge and interior compartments use in the compartmental model of Chapter 4. First we calculate the total volume of the cell, approximating a resting cell as a half-sphere of radius $5 - 10\mu$m. The total cellular volume is

$$V_{tot} = \frac{1}{2} \cdot \frac{4\pi}{3} r^3 \approx \frac{2\pi}{3} (5\text{-}10 \mu \text{m})^3,$$

and therefore,

$$V_{tot} \approx 250\text{-}2000 \mu \text{m}^3.$$

From van Rheenen (2007, 2008), we divide the cell into a periphery or edge compartment, reaching a distance $200n$m into the cell. We denote this volume as V^E. We obtain a range of magnitudes for V^E depending on assumptions about the geometric representation of this periphery compartment, that is whether data describes the periphery as a thin ring around the edge of the cell (as if a cross-section), or a thin film that covers the entire surface of the cell. (This is still to be discussed) Working with assumption 2,

$$V^E \approx \frac{1}{2} 4\pi r^2 \cdot \omega = 2\pi (5\text{-}10 \mu \text{m})^2 \cdot 0.200 \mu \text{m},$$

which gives a range of

$$V^E \approx 40\text{-}156 \mu \text{m}^3.$$

Assumption 1 would result in a much smaller value of V^E, we will work with this value for now. We will denote the volume of the interior compartment as V^I, it comprises the remaining volume fraction

$$V^I = V_{tot} - V^E \approx 200\text{-}1850 \mu \text{m}^3$$

MATLAB Code for Simulations of Temporal Model in Chapter 3

```
%% Cofilin ODE - FULL with constant filament density
clear; close all
% ---Variables---
%
% PLC = PLC normalized to PLC(rest)
% P2 = PIP2 normalized to P2(rest)
%
% C2 = Cofilin inactivated by PIP2 at membrane
% CA = Cofilin active free diffusing
% CF = Cofilin ready-to-sever filament bound
% CM = Cofilin inactivated by G-actin monomer post-severing
% CP = Cofilin inactivated by phosphate added by LIMK - freely diffusing
%
%---F = F-actin density normalized to F-actin(rest)
% B = barbed end density - active polymerizing barbed ends

% ---Parameters---

% PLC
d_plc=0.018;        % decay rate
I_stim=d_plc*1.5;   % scaled stimulation

% PIP2
d_p2=0.002;         % decay
d_hyd=0.01;
%d_hyd=0.04;        % scaled stim hydrolysis ~20*(resting decay)
psi=1;              % binding ratio of C2:PIP2
```

```
% C2
d_c2=0.002;      % base decay rate (assume = PIP2 decay)
k_dp=0.5*d_c2;      % dephos rate (onto membrane) Assume slow

% CF
k_sev=0.67/0.02*kp;        % base proportional severing rate

% CA
kp=k_dp/3.4;        % satisfy rest states
k_off=0.08;
k_onF=(k_sev + k_off)/(0.68-k_sev/kp);

% CM
%kp_Act=0.01;     % enhanced phosphorylation
%b_SSH=0.01;      % reduction in phosphorylation rate due to G-actin removal

% CP

% B
k_cap=1;        % capping rate
A=1000;         % ratio a*C_tot/B_rest

% Other
n=7;            % non-linear factor
sat=0; %1;      % saturation on/off
K=1;            % saturation coefficient

t_stim=60;      % length of stimulus
t_off=120;

CP_re=0.20;     % Song (2006)
```

```
C2_re=0.10; % discussion
CF_re=0.02;     % van Rheenen (2007)
CM_re=0.67;
CA_re=0.01; % estimate

C_rest = [C2_re CA_re CF_re CM_re CP_re];

phi_F = CF_re;

% ---Initials---

C2_check = k_dp/(d_c2)*CP_re;

CA_check = 1/(kp + k_onF)*(d_c2*C2_re + k_off*CF_re);

CM_check = k_sev/kp*CF_re;

CF_check = k_onF/(k_off+k_sev)*CA_re;

CP_check = kp/k_dp*(CA_re + CM_re); % verify match defined rest states

% B_re = alpha*k_sev/kappa*CF_re;

C_check = [C2_check CA_check CF_check CM_check CP_check];       % print resting concentrations
disp(C_check)
% ---Equations---

Fsev = @(x) k_sev*phi_F*(x./phi_F).^n;      % severing function
%Fsev = @(x) k_sev*phi_A*(x./phi_A).^n./(K^n+sat*(x./CF_re).^n);    % severing function
%Fsev = @(x) k_sev*x;
```

```
IPLC = @(x) I_stim*x;

KP_ACT = @(x) kp_Act*x;

EGF = @(x) (x>60)*(x<120);              % EGF stimulus


% ---ODEs---

% S = [PLC PIP2 C2 CA CF CM CP B T] (9)!

dSdt = @(t,S)[  IPLC(EGF(S(9))) - d_plc*(S(1)-1);

                d_p2*(1-S(2)) - d_hyd*(S(1)-1)*S(2);

                k_dp*S(2)*S(7) - d_c2*S(3) - d_hyd*(S(1)-1)*S(3);

                d_c2*S(3) - kp*S(4) - k_onF*S(4) + k_off*S(5) + d_hyd*(S(1)-1)*S(3);

                k_onF*S(4) - k_off*S(5) - k_sevb*S(5) - Fsev(S(5));

                k_sevb*S(5) - kp*S(6) + Fsev(S(5));

                kp*S(6) + kp*S(4) - k_dp*S(2)*S(7);

                %k_cap*(1-S(8)) + A*Fsev(S(5));
                %k_cap*(Fsev(S(5))/(k_sev*phi_F)-S(8));
A*Fsev(S(5)) - k_cap*S(8)
                1];                                          % system ODEs

% ---Integration---
```

```
options = odeset('abstol', 1e-28);

Sinit = [1 1 C2_re CA_re CF_re CM_re CP_re 1 0];  % initial conditions

tfinal = 300;   % final time in s

[T,S] = ode45(dSdt, [0 tfinal], Sinit, options);
```